



Original Paper

Experimental deformation of shales at elevated temperature and pressure: Pore-crack system evolution and its effects on shale gas reservoirs



Yi-Wen Ju ^{a,*,1}, Xin-Gao Hou ^{a,1}, Kui Han ^{b,**}, Yu Song ^c, Lei Xiao ^a, Cheng Huang ^a, Hong-Jian Zhu ^a, Li-Ru Tao ^a

^a Key Laboratory of Earth System Numerical Modeling and Application, College of Earth and Planetary Sciences, University of Chinese Academy of Sciences, Chinese Academy of Sciences, Beijing, 100049, China

^b Key Laboratory of Earth Exploration and Information Technique, Ministry of Education, College of Geophysics, Chengdu University of Technology, Chengdu, 610059, Sichuan, China

^c Key Laboratory of Coalbed Methane Resource & Reservoir Formation Process, Ministry of Education, School of Resources & Earth Science, China University of Mining and Technology, Xuzhou, 221116, Jiangsu, China

ARTICLE INFO

Article history:

Received 13 December 2023

Received in revised form

6 April 2024

Accepted 1 July 2024

Available online 2 July 2024

Edited by Jie Hao and Meng-Jiao Zhou

Keywords:

Shale

Deformation experiment

Microscopic structure

Pore-crack system

Shale gas reservoir

ABSTRACT

Although many studies based on naturally deformed samples have been carried out to investigate the pore-crack characteristics of shales, studies based on high temperature (T) and high pressure (P) deformation experiments, which can exclude sample heterogeneity factors, simulate deep T - P conditions, and generate a continuous deformation sequence, are still rare. In this study, shales with different deformation levels are generated by triaxial compression experiments, and methods including scanning electron microscopy, mercury injection, and gas sorption are utilized to characterize their influence factors and pore-crack characteristics. Results indicate that T is the primary factor influencing shale deformation when P is low, while P is dominant under high P conditions. At $T < 90$ °C and $P < 60$ MPa, shales undergo brittle deformation and their macropores decrease due to the compaction of primary pores, while mesopores increase because of the interconnection of micropores. At 90 °C $< T < 200$ °C and 60 MPa $< P < 110$ MPa, shales experience brittle-ductile transitional deformation, and their macro- and micropores increase because of the extension of open cracks and the plastic deformation of clay flakes respectively, while mesopores decrease dramatically. At $T > 200$ °C and $P > 110$ MPa, shales are subjected to ductile deformation, and their micro- and mesopores drop significantly due to the intense compaction in the matrix while macropores continuously increase with crack expansion. The permeability of shale increases with the degree of deformation and ductile material contents are predicted to be a key factor determining whether open microcracks can be preserved after ductile deformation. To account for these experimental results, an ideal model of micro pore-crack system evolution in deformed shales is further proposed, which can provide guidance for the exploration of shale gas resources in the deep or structurally complex zones.

© 2024 The Authors. Publishing services by Elsevier B.V. on behalf of KeAi Communications Co. Ltd. This is an open access article under the CC BY-NC-ND license (<http://creativecommons.org/licenses/by-nc-nd/4.0/>).

1. Introduction

The rock mechanical properties of shale, a type of soft rock

widely distributed on the surface of the lithosphere, are very important parameters in the field of geotechnical engineering due to their significant impacts on different aspects like mining, underground constructions, building foundations, and shale gas extraction (Liu et al., 2022; Rybacki et al., 2015, 2016; Sheng et al., 2013; Wang et al., 2018). In particular, as shale gas is playing an increasingly essential role in the energy field, a further understanding of microscopic characteristics and pore-crack structure of deformed shales is becoming more and more significant due to

* Corresponding author.

** Corresponding author.

E-mail addresses: juyw03@163.com (Y.-W. Ju), hankui@cdu.edu.cn (K. Han).

¹ Y.-W. Ju and X.-G. Hou contributed equally to this paper.

their great impact on the gas adsorption and seepage properties as well as the reservoir reconstructive ability (Guo et al., 2023; Ju et al., 2018; Ma et al., 2015; Setiawan and Zimmerman, 2018; Zhu et al., 2019). In previous cognition, structural deformation is considered to have negative impacts on the accumulation of shale gas because the development of opening fractures could lead to the decrease of reservoir pressure and shale gas escape from original reservoirs (Bowker, 2007; Guo, 2016; Liang et al., 2017). However, the edge of Sichuan Basin, which has been tectonically deformed, has been confirmed to favor the preservation and accumulation of shale gas, contributing to several economically exploited gas fields such as Fuling and Changning (Ma et al., 2020; Sun et al., 2022) (Fig. 1). Therefore, how could the shale properties be affected by structural deformation, and whether structural deformation is a direct or indirect cause of the high production of shale gas in structurally complex areas, have recently attracted attention from both tectonic geologists and geological engineers.

Studies about the influence of structural deformation on reservoir properties of shales begin with observation and analysis of naturally deformed samples, through which the impacts of deformation on shale's pore-crack structure, organic structure, percolation characteristics, fracturing characteristics, etc. are investigated (Aydin and Engelder, 2014; Gasparrini et al., 2014; Ju et al., 2018; Li et al., 2021; Liang et al., 2017; Sun et al., 2023; Zeng et al., 2023; Zhu et al., 2018, 2019). For instance, structural deformation is considered to affect shale reservoirs' pore size distribution (PSD) by increasing the proportion of macropore and micro-fractures, which could result in the decrease of their absorption capacity and the

increase of their free-gas-storage space (Li et al., 2021; Liang et al., 2017; Ma et al., 2020). Shale reservoirs with brittle, brittle-ductile transitional, and ductile deformation were identified in field, among which the brittle deformation is considered to be prone to the development of interparticle pores and micro-fractures as well as the enhancement of connectivity and porosity, while the ductile deformation is considered to cause the formation of intraparticle pores and micropores as well as the decrease of permeability and porosity (Ju et al., 2018; Zhu et al., 2018, 2019). However, although the naturally deformed shales have been observed and described at different scopes, due to the limitations of research methods, the mechanical behavior and pore-crack structure characteristics of shales under specific temperature (T) and pressure (P) conditions still lack understanding, which are urgent problems to be solved in the current situation where shale gas exploration is gradually moving towards deeper and structurally complex areas (Li et al., 2023; Ma et al., 2023).

Experimental compression at certain T - P conditions can effectively simulate the course of natural deformation, therefore being an effective method to investigate the continuous evolutionary process of the internal structure of shales during deformation (Cheng et al., 2023; Esemeh et al., 2012; Guo et al., 2023; Ibanez and Kronenberg, 1993; Wang et al., 2018; Wu et al., 2019). Ibanez and Kronenberg (1993) employed triaxial compression experiments on shales at differing confining pressures (P_c) and temperatures, through which they found that the brittle deformation occurs at $P_c < 100$ MPa while the brittle-ductile transitional deformation happens at $100 \text{ MPa} < P_c < 400$ MPa. They also found that shales

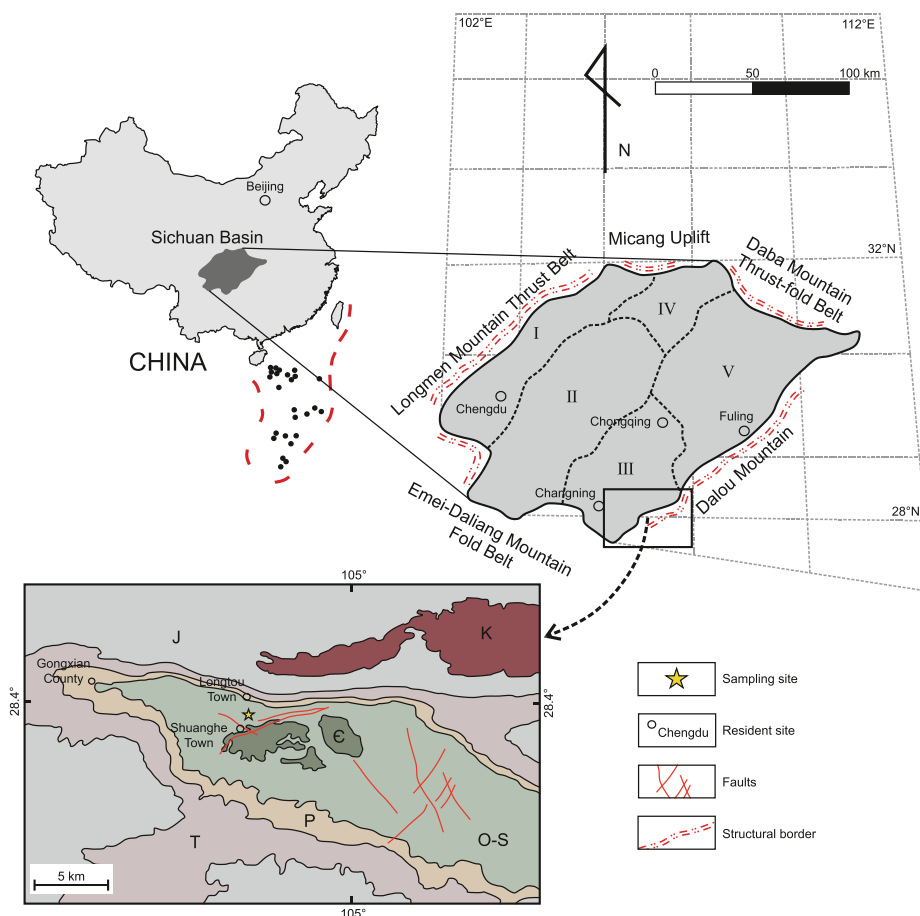


Fig. 1. Simplified geological map of the sampling locations, modified from Zhu et al. (2018). I: West Sichuan Depression, II: Central Sichuan Uplift, III: South Sichuan Low and Gentle Folding Belt, IV: Northeast Sichuan Depression, V: East Sichuan High and Steep Folding Belt.

undergo brittle-ductile transitional deformation by generating macroscopic fractures, semi-brittle shear zones, and kink bands. Besides, utilizing compression experiments, the P – T conditions for the brittle-to-ductile transition of shales were further confined to be $P_c = 75$ – 100 MPa and $T = 200$ °C (Cheng et al., 2023). In terms of pore-crack structures, the subsidence-burial and thermal maturation process of shales were simulated by deformation experiments at elevated T and P_c to examine their impacts on the evolution of pore structure and permeability (Eseme et al., 2012; Wu et al., 2019). The X-ray computed tomography was used to investigate micro-structures and fractures formed after triaxial compression tests as well (Uehara and Takahashi, 2014; Wang et al., 2018). Moreover, the creation and propagation of microcracks that occur during experimental deformation were calculated and characterized mathematically by simplifying shale as a homogenous material (Eberhardt et al., 1998; Zavattieri and Espinosa, 2001). Furthermore, experiment and computer simulation results were also used to build models of apparent permeability in shales (Xu et al., 2017, 2019). However, although previous studies have already invested a lot of effort in this field, the relationship between deformation conditions and some crucial parameters for defining target areas of shale gas exploration (i.e., PSD, specific surface area (SSA), pore volume, etc.) is still poorly understood, and the evolutionary process of the microscopic pore-crack structure of shales accompanied by structural deformation still needs further discussion.

In this study, high- T and high- P triaxial compression tests were applied to natural undeformed shale samples. Characteristics of pores and microcracks of shales before and after deformation were observed with scanning electron microscopy. The organic petrography, low-temperature N_2 and CO_2 adsorption, and mercury injection tests carried out in this study as well as published data were comprehensively studied to investigate the pore-crack structure of deformed shales, of which results are beneficial for further exploration of shale gas resource.

2. Methodology

2.1. Sample selection

The sampling site is located at the South Sichuan Low and Gentle Folding Belt of Sichuan Basin, China, where the north wing of the Changning anticline is partly exposed (Fig. 1). The target layer, Wufeng Formation of Upper Ordovician, is in conformable contact with the overlying Guanyinqiao Formation with clear stratification in the sampling site, indicating weak structural modification. Although located within the Changning anticline, the shale does not exhibit significant deformed structures such as folds, fractures, slickenside, or mylonite, which are widely presented in the east of the Sichuan Basin (Ma et al., 2014; Yan et al., 2003). In order to ensure that the collected sample can represent the undeformed shale as much as possible, a blocky shale rock of $1\text{ m} \times 1\text{ m} \times 15\text{ cm}$ with hard texture, clear banding, large layer thickness, and well-preserved primary structures such as bedding, was selected for the follow-up experiments after removing apparent weathering layer.

2.2. Mineralogical composition and organic petrography analysis

Before compression tests, a small proportion of the undeformed blocky shale sample was removed and used for petrologic and mineralogical parameter testing. The sample was ground into powder with an average particle size of 60–80 mesh and then smear mounted on glass slides for random-powder X-ray diffraction (XRD) analyses with a D/Max-TTRIII analyzer, following the

procedures outlined in Hillier (1999). The measurement of random reflectance (R_0) of the shale sample was conducted using a 3Y-Leica DMR XP microscopy equipped with a microphotometer (MPV-3). Total organic carbon (TOC) content was quantified using a LECO CS-230 carbon and sulfur analyzer with an accuracy within 0.5% after the powdered samples were treated by hydrochloric acid (1:7 of HCl:H₂O) at 60 ± 5 °C to remove carbonates. The porosity and permeability of the sample were analyzed using an Ultrapore-200A Helium porosimeter and an ULTRA-PERMTM20 permeability instrument.

2.3. High-temperature and high-pressure triaxial compression experiment

Before compression tests, the weathering layer of the undeformed blocky shale sample was further removed in a laboratory environment to guarantee the sample used for tests was fresh. Then, several shale cylinders, each of which is $20 (\pm 0.2)$ mm in diameter and $40 (\pm 0.2)$ mm in length (Fig. 2), were extracted from the undeformed blocky shale sample by a drill. To minimize the impact of sample heterogeneity, all prepared shale cylinders were drilled perpendicularly to the bedding and closely with each other within a relatively confined and uniform area.

The high-temperature and high-pressure triaxial compression test was run on a high-temperature and high-pressure gas medium triaxial test system with argon as the gas medium in the Laboratory of Tectonophysics, Institute of Geology, China Earthquake Administration. A YAMATAKE DCP30 temperature controller was used to control temperatures, and a digital hydraulic servo machine was used to control the axial pressure. More details about this experimental apparatus can be found in previous studies (He et al., 2006; Xu et al., 2014; Zhang and He, 2013). Before compression, shale samples were placed in a drying oven and dried at 120 °C for 24 h for dehydration. Given the average geothermal gradient of 3 °C/100 m as well as the suggested burial depth with a maximum of 7000 m throughout the diagenesis and tectonic evolution history of the Wufeng Formation (Cao et al., 2015), the temperatures in this test are set from the atmosphere ($T = 25$ °C) up to $T = 200$ °C with varying intervals. The range of 60–110 MPa is applied to the confining pressure (P_c) concerning the unpredicted lateral tectonic stress. Besides, two relatively higher temperature-pressure conditions of ($T = 300$ °C, $P_c = 160$ MPa) and ($T = 300$ °C, $P_c = 200$ MPa) were designed to further explore the ductile deformation characteristics of shales.

During the experiment, the axial pressure and P_c were first applied synchronously according to a certain proportion. When the P_c reached the set value, the displacement control was switched to pressure control, and the heating began after P_c stabilized. Constant pressure control can ensure that the expansion of the sample during heating will not change the P_c condition during heating. The accuracy of T and P_c were controlled within ± 1 °C and 0.5 MPa, respectively. After the T and P_c reached pre-set values, the deformation experiment of shale started by axial loading. The loading of axial compression was controlled by constant displacement rates, which were 1×10^{-5} m/s, 0.2×10^{-5} m/s, and 0.04×10^{-5} m/s, with stepping strain rates varying from 2.5×10^{-4} s⁻¹, 5×10^{-5} s⁻¹, and 1×10^{-5} s⁻¹, successively. Using different displacement rates in compression experiments helps to calculate the relevant rheological coefficients for ductile deformation in subsequent discussions. The setting data and results of compression experiments are assembled in Table 1, Figs. 2, and Fig. 3.

2.4. Scanning electron microscopy test

Microstructures of both undeformed and deformed shales were

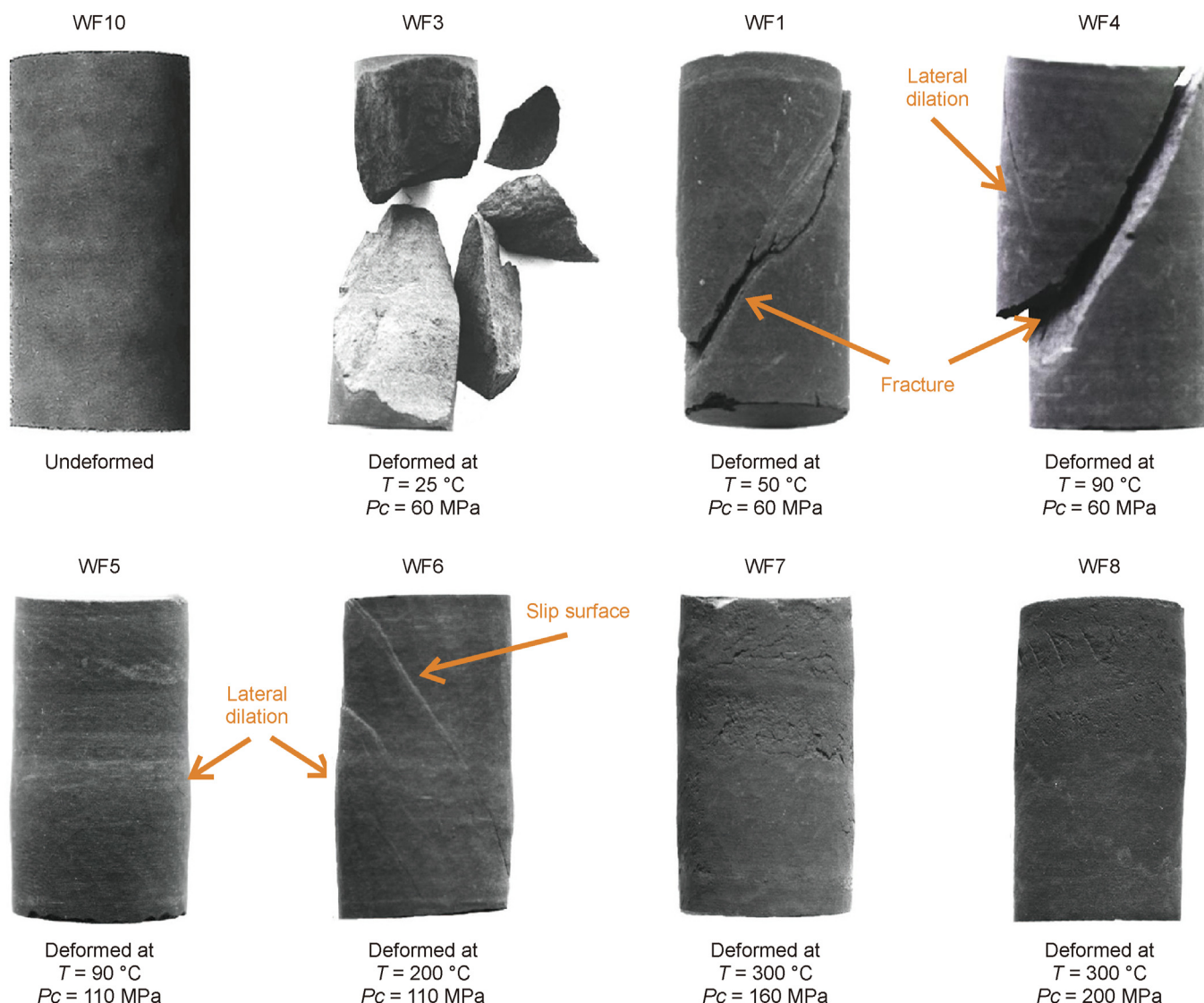


Fig. 2. Images of shale samples deformed after different conditions.

observed by optical microscopy and ultrahigh-resolution FE-SEM (field emission-scanning electron microscopy). To make the surface morphology of the sample more realistic and clearer, after mechanical polishing, the Broad Ion Beam Milling, which has been widely adapted to fine-grain shale treatment (Klaver et al., 2012; Loucks et al., 2012; Wang et al., 2009), was used to repolish the sample surface without water. Observation experiments were performed at NOVA® NanoSEM 430 in the Electron Microscopy Laboratory of Peking University and at SUPRA55 SAPPiRE at China University of Geoscience (Beijing). To describe the microscopic characteristics of shale, pore classification and the definition of pore characterization as proposed by Loucks et al. (2012) are used (i.e., interparticle pore, intraparticle pore, and organic matter (OM) pore).

2.5. Mercury intrusion porosimetry, low-temperature N_2 adsorption, and CO_2 adsorption

Quantitative information implying the pore-crack structure was extracted by the combined application of mercury intrusion porosimetry (MIP), low-temperature nitrogen (N_2) adsorption, and

carbon dioxide (CO_2) adsorption. Among them, MIP was employed to provide PSD data using a Micromeritics® HG 9405 Series at the temperature of 18 °C and relative humidity of 50% as well as injection pressures of up to 300 MPa and the measured pressure range equates to the pore diameter range of 3 nm–200 μm , based on the SY/T5346-2005 standard in China. Other parameters like total pore volume, SSA, porosity, etc., were not measured by MIP as their measurements after the loading test were no longer consistent with the demand for standard MIP procedure.

Given that the data of MIP are not precise for the micropores (Mastalerz et al., 2013; Zhu et al., 2019), low-pressure gas adsorption analyses have also been used to measure the PSD of both micropores and mesopores using both N_2 adsorption at 77.35K (−196 °C) and CO_2 adsorption at 273.15K (0 °C) by a Quantachrome® Autosorb IQ. Before the experiments, samples were crushed to 60–80 mesh, dehydrated for 5 h at 110 °C, and then outgassed for 24 h at 110 °C. Besides, pore structure parameters, including pore volume, SSA, and pore diameter (mode), are calculated based on multiple adsorption theories, i.e., Brunauer-Emmett-Teller (BET), Barrett-Joyner-Halenda (BJH), density functional theory (DFT), and Dubinin-Radushkevich (D-R). Detailed descriptions of these

Table 1
Setting and results of shale deformation experiments.

Sample number	Temperature, °C	Confining pressure, MPa	Displacement rate, 1×10^{-5} m/s	Strain rate, s^{-1}	Differential stress, MPa	Strain, %	α , MPa^{-1}
WF3	25	60	1	2.5×10^{-4}	212	6.54	
			0.20	5×10^{-5}	206	7.49	
			0.04	1×10^{-5}	203	7.80	
WF1	50	60	1	2.5×10^{-4}	206	6.18	
			0.20	5×10^{-5}	202	7.17	
			0.04	1×10^{-5}	199	7.99	
WF4	90	60	1	2.5×10^{-4}	205	6.89	
			0.20	5×10^{-5}	204	8.24	
			0.04	1×10^{-5}	203	8.88	
WF5	90	110	1	2.5×10^{-4}	299	6.96	0.54
			0.20	5×10^{-5}	297	8.26	
			0.04	1×10^{-5}	293	9.13	
WF6	200	110	1	2.5×10^{-4}	338	8.76	0.11
			0.20	5×10^{-5}	333	10.34	
			0.04	1×10^{-5}	310	11.72	
WF7	300	160	1	2.5×10^{-4}	455	11.87	0.10
			0.20	5×10^{-5}	435	12.9	
			0.04	1×10^{-5}	424	13.45	
WF8	300	200	1	2.5×10^{-4}	505	11.78	0.16
			0.20	5×10^{-5}	490	12.41	
			0.04	1×10^{-5}	485	13.05	

The detailed calculation process of α can be found in Ibanez and Kronenberg (1993). The α values of WF3, WF1, and WF4 are unavailable because they did not reach steady-state rheology.

theories can refer to Gregg and Sing (1982). Low-temperature N_2 adsorption data were used to represent mesopores and partial macropores (uniformly referred to as mesopores thereafter) because preliminary studies have pointed out that the employment of N_2 adsorption should be restricted to the pores with wider than 2 nm, owing to the incapability of N_2 and lack of required energy to access the micropore at low temperature (Gan et al., 1972; Ross and Bustin, 2009). In contrast, CO_2 molecules have a relatively small diameter and thermal energy, and consequently, CO_2 adsorption data were used to calculate the aforementioned parameters of micropores (Bustin et al., 2008; Wang et al., 2015b). It should be noted that pores mentioned here follow the International Union of Pure and Applied Chemistry (IUPAC) that classifies the pores into three types: micropore (<2 nm), mesopore (2–50 nm) and macropore (>50 nm). The result is presented in Table 2.

3. Results and discussion

3.1. Rationality of experimental design

To study the effects of deformation on the pore-crack structure evolution of shales by experimental simulation, it is necessary to discuss to what extent compressional experiments can represent the natural deformation processes. Previous studies have suggested that factors including rock composition (organic and inorganic), burial, deposition, compaction, dissolution, and hydrocarbon generation can all influence the pore-crack structure of shale (Chalmers et al., 2012; Li et al., 2021; Loucks et al., 2012; Schieber et al., 2000; Slatt and O'Brien, 2011; Zhu et al., 2019). Given that all samples are collected from a very restricted section as mentioned above, these inner factors can be considered as

constants in this study. In terms of mineralogical composition, the results of XRD analysis show that quartz has the highest content, accounting for 46.4% of the total inorganic components, followed by clay minerals, accounting for 25.0%, calcite accounts for 16.9%, dolomite accounts for 10.7%, and albite only accounts for 1.0%. No K-feldspar was detected in this shale sample. Besides, organic petrography analysis shows that the average R_o value of OM reaches 2.31%, and the TOC value reaches approximately 4.06%. The porosity of the undeformed shale sample is analyzed to be as high as 17.57%, while the permeability is merely 0.012 mD. Such parameters mentioned above are revealed to be in good agreement with previous studies (Tan et al., 2014; Wang and Ju, 2015), indicating that the sample is representative of the Wufeng Formation shale. Moreover, although the strain rate during the actual geological deformation process is too low (10^{-12} – 10^{-17} m/s) to simulate in laboratory conditions, the equivalence between heating up and reducing strain rate has been reported (Stocker and Ashby, 1973). Thus, the experimental temperatures of WF7 and WF8 were raised accordingly as control groups to compensate for the relatively short deformation time. To sum up, the compressional experiments in this study are considered to be capable of representing the natural deformation processes to a certain extent.

3.2. Experimental deformation of shales

3.2.1. Macroscopic deformation characteristics of shales

Undeformed sample (WF10) and deformed samples (WF3, WF1, WF4, WF5, WF6, WF7, WF8) are presented in Fig. 2. The strongest rupture occurs in WF3, which has broken into several parts and no lateral dilation has been observed when reintegrating these pieces (Fig. 2). Both WF1 and WF4 rupture at approximately 45° to the axis

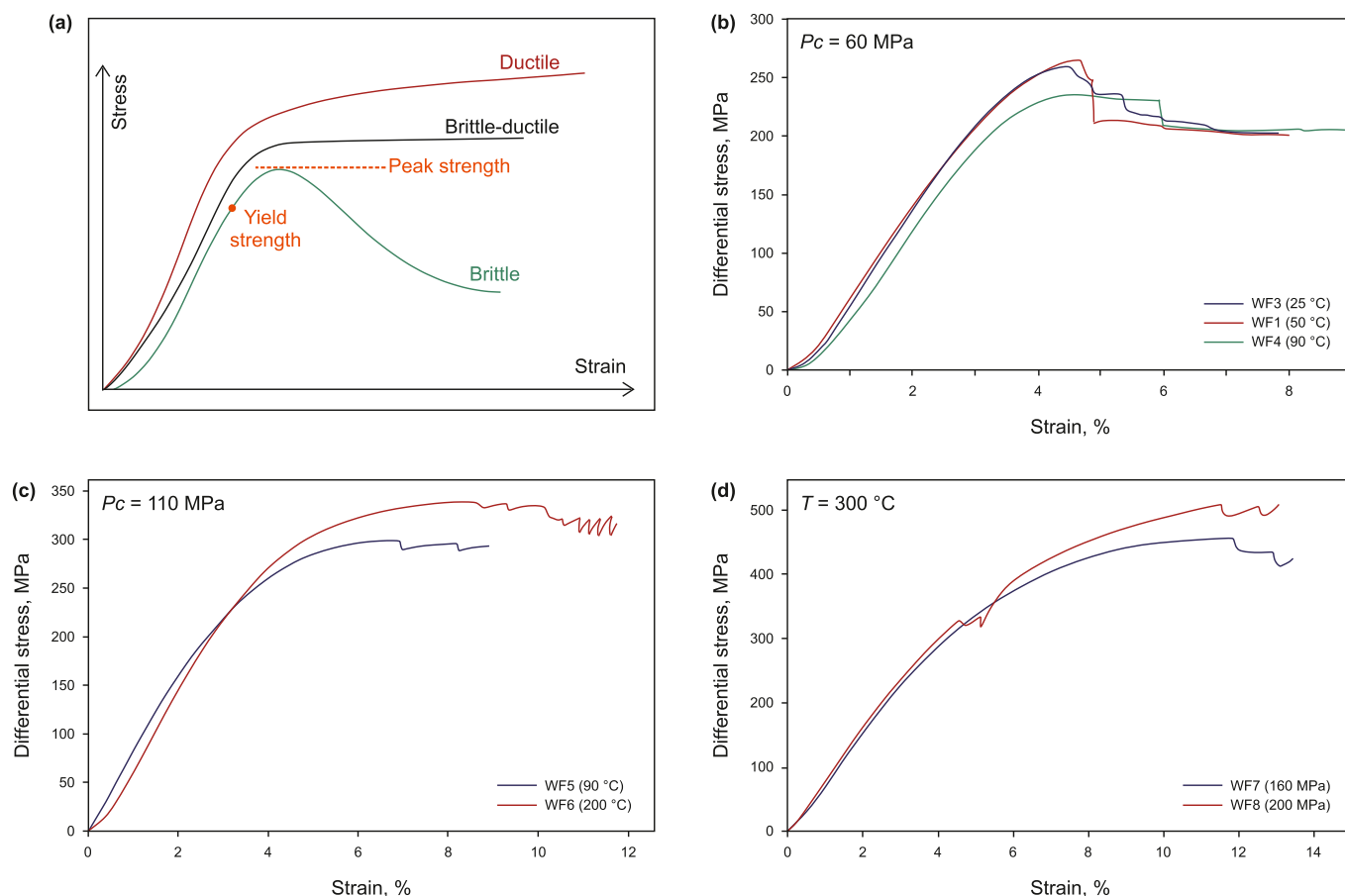


Fig. 3. Stress-strain curves of (a) typical deformation types of rock; (b) shales deformed at 60 MPa; (c) shales deformed at 110 MPa; and (d) shales deformed at 300 °C.

Table 2
Pore-crack parameters of shales with different levels of deformation.

Sample number	Mesopore			Micropore		
	N ₂ BJH pore volume, 10 ⁻³ cm ³ /g	N ₂ BET specific surface area, m ² /g	N ₂ BJH pore diameter (mode), nm	CO ₂ D-R pore volume, 10 ⁻³ cm ³ /g	CO ₂ D-R specific surface area, m ² /g	CO ₂ DFT pore diameter (mode), nm
WF10	25.76	16.640	3.930	5	12.280	0.349
WF3	26.20	13.400	3.930	5	14.272	0.822
WF1	33.84	20.078	3.926	4	9.9430	0.501
WF4	29.60	16.830	3.926	1	4.749	0.349
WF5	22.35	11.400	3.929	4	11.296	0.479
WF6	21.36	7.985	3.966	2	7.060	0.524
WF7	30.67	6.647	3.968	2	6.329	0.349
WF8	16.84	9.164	3.976	0	1.660	0.524

of the shale cylinder, but unlike WF1, which exhibits pure brittle fracturing, WF4 dilates slightly in the radius direction (Fig. 2). WF5, WF6, WF7, and WF8 all exhibit deformation characteristics of non-brittle deformation and lateral dilation, while there are still distinct features among them. Compared with WF5, WF7, and WF8, two significant slip surfaces are developed in WF6 (Fig. 2), which might result from some potential weak planes caused by sample heterogeneity. In addition, WF7 and WF8 exhibit more uniform dilation along the cylinder axis and present a remarkable dehydration phenomenon, manifested by the occurrence of water remaining in the sample jacket after compression tests as well as the generation of capillary fissures. This might be the result of the loss of interlayer water or molecular H₂O absorbed on the clay mineral surface. To sum up, the deformation behavior of shales shifts from ruptural to

plastic with *T* and *P_c* increase.

3.2.2. Classification of deformation types of shales

In field studies, the deformation types of naturally deformed shale are usually classified into brittle and ductile (Zhu et al., 2018), or brittle, brittle-ductile transitional, and ductile (Ju et al., 2018; Li et al., 2021; Zeng et al., 2023; Zhu et al., 2019). However, it is much easier to classify these deformation types in naturally deformed samples than experimental ones, as the deformation of natural samples is usually linked to specific structures. For example, brittle-deformed rocks are represented by joints, faults, and fracture zones, while ductile-deformed rocks are usually represented by folds and ductile shear zones. In contrast, the volume of experimental samples is relatively too small to generate significant structures,

especially in the ductile deformation domain (Fig. 2). Therefore, it is crucial to classify the deformation levels of these experimentally deformed shales before further discussion.

The deformation type can be distinguished from stress-strain diagrams (Guo et al., 2023; Lei et al., 2023) (Fig. 3). In the initial stage of deformation, stress, and strain follow Hooke's law and exhibit a linear positive correlation, thus belonging to elastic deformation. When a certain stress value (yield strength) is exceeded, the slope of the stress-strain curve starts to gradually decline, corresponding to plastic deformation. During brittle deformation, the stress-strain curve would drop rapidly soon after the end of the elastic stage (Fig. 3(a)). As the degree of deformation increases, the sample enters the brittle-ductile transitional or ductile deformation regime, showing a gradual decrease in the slope of the stress-strain curve, and there is no longer a linear positive correlation between stress and strain. When the slope of the stress-strain curve approaches zero, we say that the sample undergoes steady-state rheological behavior, which can be considered as a symbol of brittle-ductile transitional deformation (Fig. 3(a)). If both stress and strain continue to rise and the slope shows a decreasing trend, we believe that the sample has undergone ductile deformation (Fig. 3(a)).

In this study, WF1 and WF3 exhibit relatively short plastic deformation stages, rupturing soon when the strain rate reaches about 4.5% (Fig. 3(b)). WF4 also shows intense rupture, but it has experienced a period of steady-state rheology with longer plastic deformation stage and does not rupture until the strain rate reaches about 6% (Fig. 3(b)). WF5 and WF6 both exhibit a noticeable longer plastic deformation stage with the peak strength around 300 MPa (Fig. 3(c)), but WF6 exhibits a unique zigzag pattern at the end of the compression test. The curves of WF7 and WF8 exhibit both elastic and plastic stages (Fig. 3(d)). Before the first shift of strain rate, WF7 has almost reached a steady-state rheological state and its peak strength is about 450 MPa. By comparison, the curve of WF8 exhibits no obvious steady state but a continuously increasing trend, indicating great potential for further deformation with a peak strength of around 550 MPa.

Combining characteristics of stress-strain curves and macroscopic observations, we can easily identify that WF3 and WF1 have experienced typical brittle deformation. The deformation type of WF4 is by comparison more complicated, featured by the coexistence of shear fracture and lateral dilation (Fig. 2). Given that it displays steady-state rheology in the stress-strain diagram, we infer that its deformation may be brittle-ductile transitional rather than purely brittle. WF5, WF6, and WF7 have all experienced a period of steady-state rheological stage (Fig. 3), which is consistent with their lateral dilation features formed during compression tests. WF8 has not reached steady-state rheology before the first strain rate shift, demonstrating that there is still a large amount of space for plastic deformation (Fig. 3(c)). In summary, combined with the condition for brittle-to-ductile deformation transition ($P_c = 75\text{--}100$ MPa, $T = 200$ °C) proposed by Cheng et al. (2023), the deformation of WF7 and WF8 is supposed to be ductile, and that of WF4, WF5, and WF6 is considered to be brittle-ductile transitional, while that of WF3 and WF1 is classified to be brittle.

3.2.3. Controlling factors of deformation behavior of shales

The deformation characteristics of rocks in compression experiments are extensively understood to be affected by factors including temperature, confining pressure, rock property, strain rate, etc. (Guo et al., 2023; Herrmann et al., 2018; Ibanez and Kronenberg, 1993). In this study, because the inherent properties of shales, including the composition, fabric, texture, type of crystal lattice, etc. Which can considerably affect the rock deformation behavior, are believed to be almost the same as argued above, the

impacts of external conditions including T and P_c can be investigated.

When treating temperature as a variable (Fig. 3(b)), in the group with $P_c = 60$ MPa (WF3, WF1, and WF4), WF3 ($T = 25$ °C) and WF1 ($T = 50$ °C) display almost the same stress-strain curves with peak strength around 260 MPa, while WF4 deformed under higher temperature ($T = 90$ °C) shows significant decrease in peak strength (about 230 MPa) and longer plastic deformation stage. Nevertheless, in the group with higher pressure condition ($P_c = 110$ MPa), the increase of temperature from 90 °C to 200 °C is conversely accompanied by the rise of peak strength (Fig. 3(c)). By comparison, when treating P_c as a variable, in groups with both high temperature ($T = 300$ °C) and relatively low temperature ($T = 90$ °C), it is apparent that the rise of peak strength and ductile deformation level always come along with the enhancement of P_c (Fig. 3(b), (c), (d)). A possible explanation is that, under the condition of low P_c , high temperature can effectively affect the deformation behavior of shale, but when a certain P_c threshold is exceeded, the temperature would lose its efficacy (Guo et al., 2023). The result is also in good agreement with previous studies, which proved that the effect of temperature on the mechanical behavior of shale is relatively weak compared with that of pressure (Ibanez and Kronenberg, 1993; Paterson, 1990). Although the high temperature has also been found to be capable of activating the generation of CO out of OM, which can enhance the shale ductility (Xu et al., 2014), this factor has not been taken into account in this paper due to the limited content of OM (4.06%).

For further investigating the effect of temperature on the strain rate of shale, three levels of displacement rate are applied to each sample (Table 1). An approach to express the strain rate and temperature sensitivity of rocks deforming by dislocation glide is an exponential law of the following form (Ibanez and Kronenberg, 1993):

$$\dot{\epsilon} = A \cdot \exp(\alpha(\sigma_1 - \sigma_3)) \cdot \exp(-Q/RT)$$

where $\dot{\epsilon}$ is the strain rate, $(\sigma_1 - \sigma_3)$ is the differential stress, Q is the activation energy, R is the ideal gas constant, T is the absolute temperature, and α is a material parameter that determines the sensitivity of strain rate to differential stress under a certain temperature. Note that the flow law listed above is valid only at steady-state rheological conditions (Rybacki et al., 2015), thus is not applicable in brittle-deformed samples. In the present study, α values are determined by plotting values of $(\sigma_1 - \sigma_3)$ and $\dot{\epsilon}$ at different strain rates, of which the detailed calculation process can be found in Ibanez and Kronenberg (1993). As shown in Table 1, the α value of WF5 with lower temperature ($T = 90$ °C) is higher than those of WF6, WF7, and WF8, of which temperature conditions are relatively higher ($T = 200\text{--}300$ °C), indicating that the same differential stress can generate relatively greater strain rate in low-temperature environments compared to high-temperature environments. This also indicates that the influence of temperature on the mechanical behavior of shale is greater under low- T conditions than under high- T conditions.

3.3. Microstructural response in experimentally deformed shales

3.3.1. Pore-crack characterization from SEM imaging

Pore-crack structure, morphology, and structural characteristics of minerals and OM, as well as cement between mineral particles and its degree of cementation in shales with different deformation levels (WF10, WF1, WF4, WF5, and WF8), were observed and described under FE-SEM. The undeformed shale (WF10) is characterized by great integrity without obvious microcrack development or mineral directional arrangement found under FE-SEM.

Pores of various shapes and sizes are mainly distributed in isolation (Fig. 4(a)). The boundary areas of mineral particles or primary pores are generally smooth, and the soft matrix between rigid particles is primarily made up of well-cemented clay minerals and OM without cracking or instability (Fig. 4(b), (c), (d)). The primary pores formed by dissolution due to carboxylic and phenolic acids created by decarboxylation during the diageneses, including dissolution intraparticle pores and dissolution-rim intraparticle pores, still remain integrity.

In terms of deformed shales, WF1 exhibits poor development of microcrack and no development of mineral lineation or cataclastic flow (Fig. 5(a)). Most pores are developed at the edges of mineral particles, which are relatively isolated from each other and have poor connectivity (Fig. 5(a)). A few microcracks develop in the organic matrix, especially where OM is continuously distributed (Fig. 5(c)). The microstructure of WF4 is generally similar to that of WF1, but the instability of mineral particle boundaries is more significant, and microcracks begin to connect non-adjacent pores on a small scale (Fig. 5(b)). In WF5 with much stronger deformation, microcracks are highly developed with a maximum width of 1–2 μm and extended generally in the same direction (Fig. 5(d) and

6(a)). These microcracks are mainly generated within the matrix by cracking clay minerals or weak OM and tearing or even penetrating rigid particles when encountering them (Fig. 6(b)). In WF8 with the strongest deformation, the highest degree of microcrack development is observed, and the extension of microcracks are visible in a large-scale range. Besides, some microcracks have also been found to form by disconnection between clay minerals and rigid minerals along the particle boundaries (Fig. 6(c), (d)). In summary, experimentally deformed shales are overall characterized by the generation and extension of microcracks and interconnection of pores in SEM images. Compared with naturally ductile-deformed rocks, within which a series of typical plastic deformation structures, such as the S–C fabric, pressure shadow, domino structure, eyeball structure, rumpled fold, pudding structure, mineral lineation, etc., can always be found (Antonellini et al., 1994; Eichhubl et al., 2005; Erickson, 1994; Needham, 2004; Schulmann et al., 1996), these rheological characteristics are not noticeable in experimentally deformed shales in this study. This may be because the experimental rock samples are controlled within a certain range with strong limitations on lateral displacement generated by the specimen jacket and loading chamber during the experimental

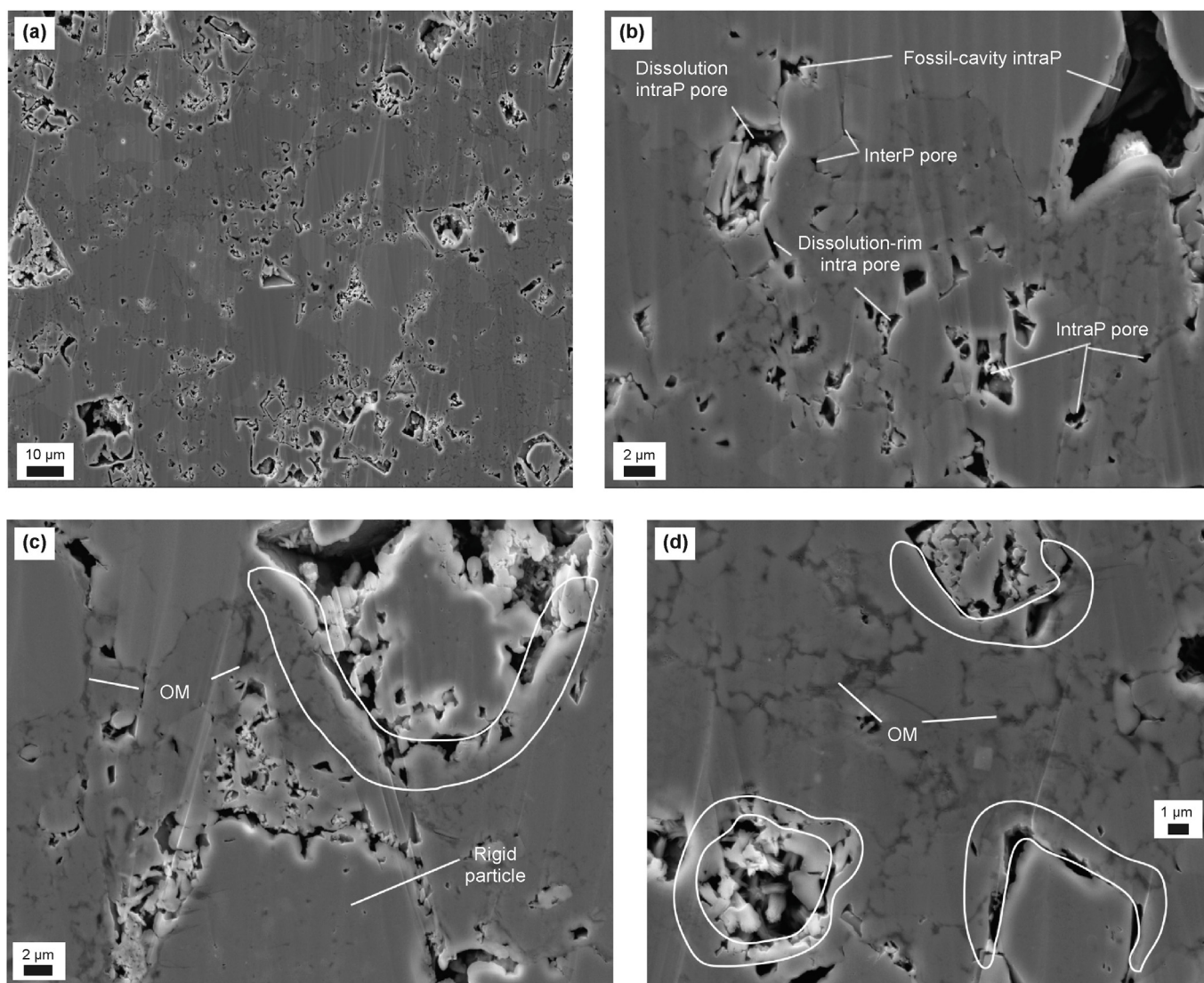


Fig. 4. BIB-FE-SEM images of microstructures in undeformed shale sample (WF10). (a) Overall microstructure characteristics of undeformed shale; (b, c, d) features of OM distribution as well as the internal textures and boundary areas of rigid particles. Circled areas display the boundary areas of rigid minerals, showing high levels of cohesion.

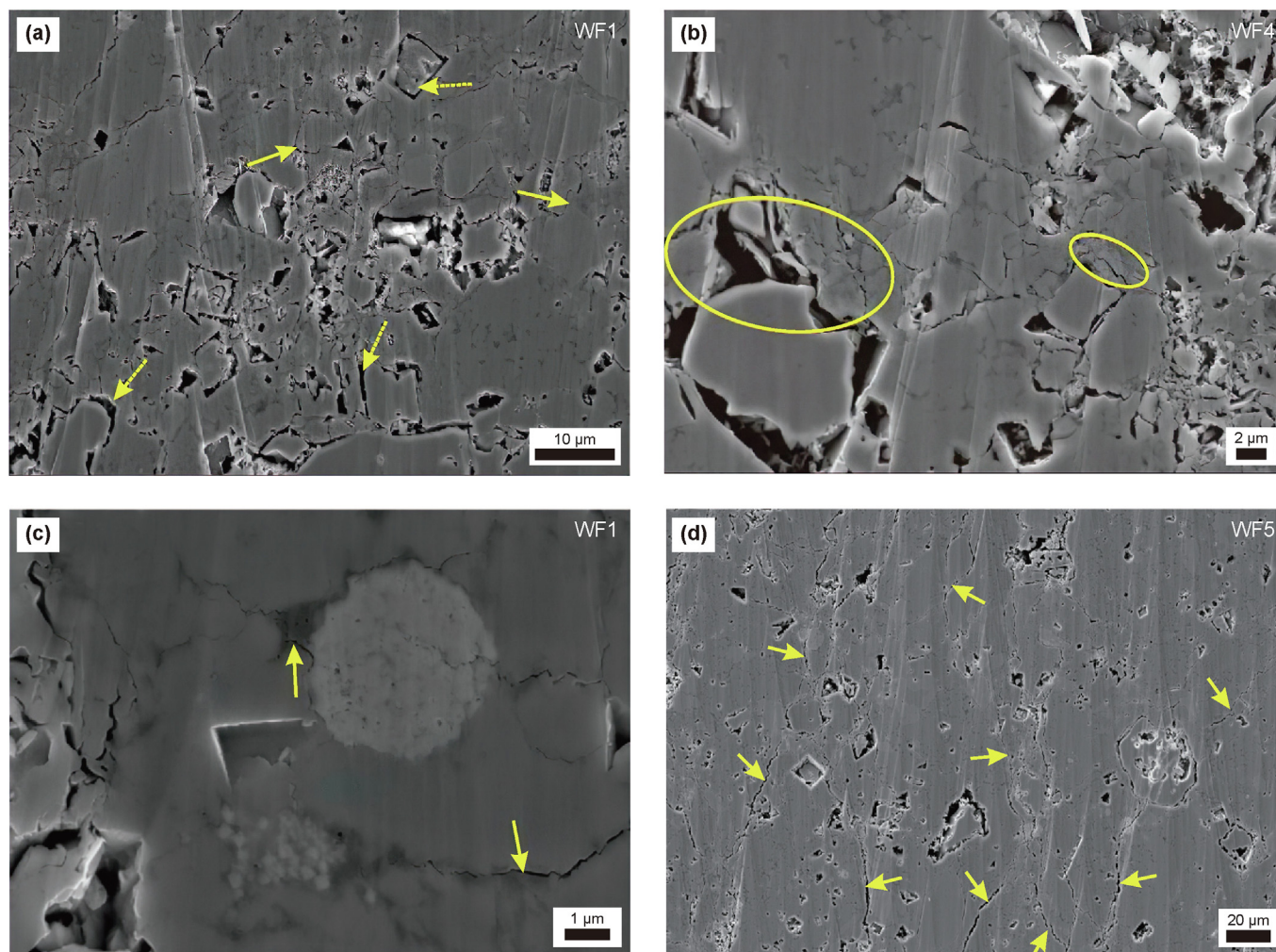


Fig. 5. BIB-FE-SEM images of deformed shales (WF1, WF4, and WF5). **(a)** Overview of the micro pore-crack structure in WF1; **(b)** boundary instability around rigid particles in WF4; **(c)** propagation of microcracks along OM in WF1; **(d)** overview of the micro pore-crack structure in WF5. Yellow dashed arrows represent primary dissolution-rim pores around mineral particles; yellow solid arrows represent microcracks induced by experimental deformation; yellow circles represent unstable boundary areas of mineral particles.

deformation process, which prohibited them from generating structures that need sufficient displacement space.

3.3.2. Classification of microcracks in experimentally deformed shales

Pores and microcracks are two important elements in shale that can provide storage space as well as migration pathways for gas molecules through the shale. With electron microscope technology, previous studies have proposed several schemes for grouping different pores based on their geometry, host minerals, or formation mechanism in natural shales (Desbois et al., 2009; Heath et al., 2011; Loucks et al., 2012; Slatt and O'Brien, 2011; Zhu et al., 2018). In contrast, the discussion of microcrack classification, which is very important for understanding the microstructure changes of shale during deformation, is relatively rare. Loucks et al. (2012) supposed that microcrack is a kind of pore controlled by more than two kinds of materials. Both Slatt and O'Brien (2011) and Zhu et al. (2018) classified microcracks in shale into micro-fracture and micro-channel. In the present study, with the advantage of experimental deformation simulation and SEM imaging, we would like to propose a classification scheme for shale microcracks (Fig. 7).

According to the positions of microcrack development, we define four types of microcrack that are generated during

experimental deformation, namely the clay microcrack, organic matter microcrack, penetration microcrack, and boundary microcrack, respectively (Fig. 7). Among them, the clay microcrack and organic matter microcrack are both developed within the matrix and dispersed with net-like shape and narrow width, while the former occurs within or between clay mineral aggregates (Fig. 7(c), (d)), and the latter develops on the interior of OM (Fig. 7(a), (b)). The penetration microcrack refers to those microcracks that cut through rigid particles or particle aggregates (Fig. 7(g), (h)). This type of microcrack was not observed in WF10, WF1, and WF3. In WF4, the penetration microcracks were only found in mineral particles affected by dissolution. Even in WF7 and WF8 with high levels of deformation, many rigid particles are not involved in the generation of penetration microcracks, especially for those located where the adjacent microcracks are absent, indicating the formation of penetration microcracks is a pure mechanical fracture process. The boundary microcrack is an epigenetic microcrack formed at the boundary of rigid particles by fracturing (Fig. 7(e), (f)). Different from original dissolution-rim pores, these epigenetic boundary microcracks are in a more regular shape, and both sides of them are more unsmooth, suggesting the absence of fluid-mineral interaction. More significantly, the boundary microcrack usually extends out and proceeds into surrounding parts along its

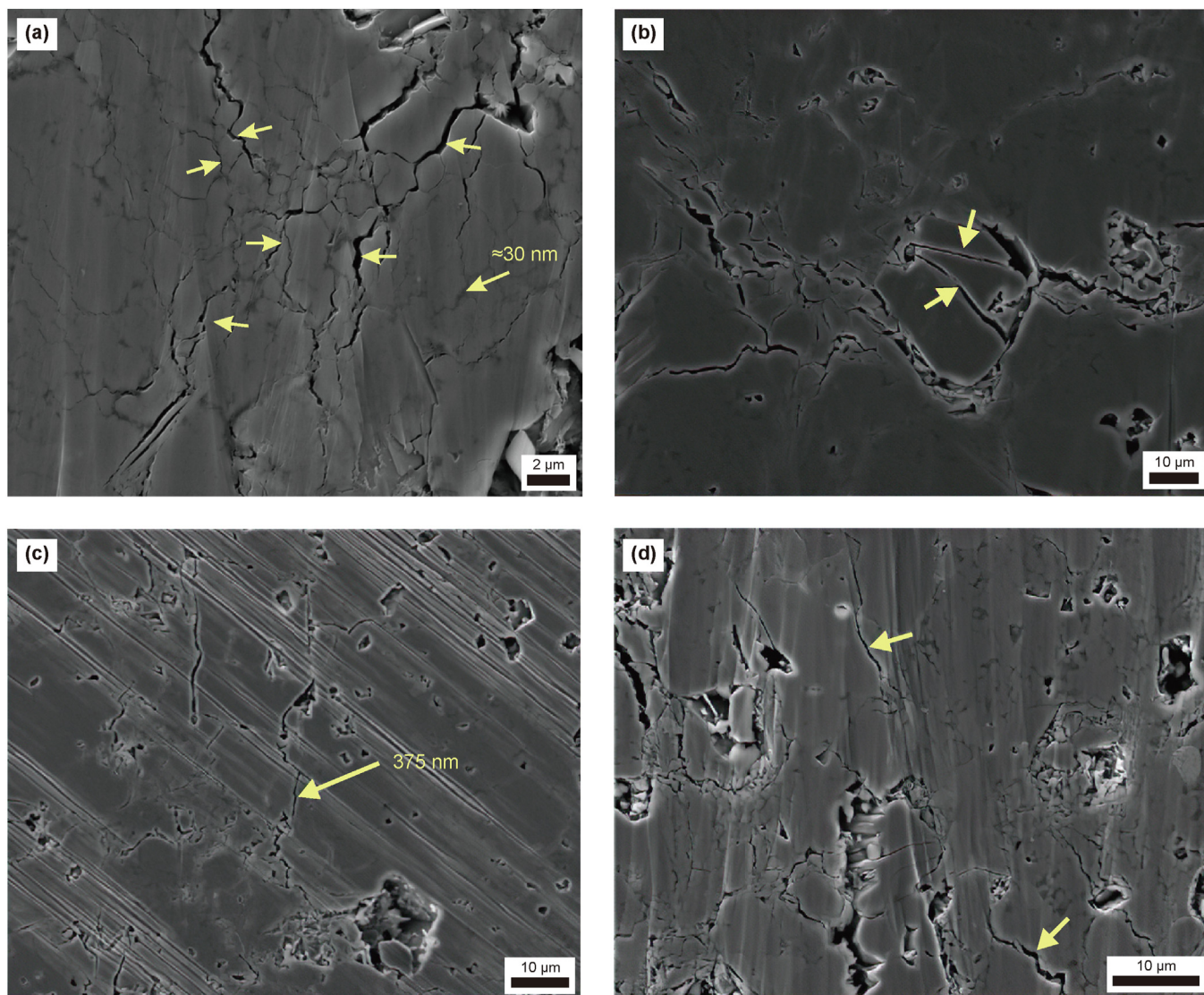


Fig. 6. BIB-FE-SEM images of deformed shales (WF5 and WF8). (a) Microcracks propagate within the matrix in WF5; (b) microcracks propagate by cutting through rigid minerals in WF5; (c, d) micro pore-crack structure in WF8 with the highest deformation level. Yellow solid arrows represent microcracks induced by experimental deformation.

orientation. With the increase of deformation degree, different types of microcracks in shale are interconnected to form relatively larger microcracks along the principal stress direction expanding up to hundreds of μm in length, ranging from a few hundred nm to a few μm in width, usually cutting through rigid minerals, and can be significantly observed through microscopy. Therefore, we further generally term this kind of microcracks as major microcracks (Fig. 7(i), (j)).

3.4. Relationship between microstructure-related parameters and deformation levels

3.4.1. Pore size distribution of deformed shales

The pore size distribution (PSD) is one of the most important properties when characterizing porous materials for gas storage. It is worth noting that, the “pore” mentioned in PSD or other parameters like pore volume and pore diameter means “void” space in shales, so epigenetic microcracks generated by deformation are also included. In the present study, the PSDs in the range of meso- and macropores of shales with different deformation levels are

characterized by MIP data (Fig. 8). Both the undeformed shale (WF10) and brittle-deformed shales (WF3 and WF1) exhibit PSD characteristics centralizing in the range of mesopore, and pores with the highest frequency in WF10 (25–40 nm) are slightly larger than those in WF1 and WF3 (16–25 nm) (Fig. 8(a)). In contrast, the PSD characteristics of shales after ductile and brittle-ductile transitional deformation (WF4, WF5, WF6, and WF8) show overall higher peaks centering at 40–63 nm (Fig. 8(b)). The proportion of macropores increases while that of mesopores decreases notably.

PSD characteristics of micropores and mesopores are characterized utilizing CO_2 adsorption and N_2 adsorption, respectively (Fig. 9). In the range of mesopores, only one peak (about 5 nm) is shown. As the deformation type shifts from brittle to brittle-ductile transitional, and then to ductile, the pore volume of mesopores decreases significantly, which is consistent with MIP results (Fig. 9). In comparison, in the range of micropores, the pore diameter of almost all samples exhibits the multimodal nature of three peaks, representing 0.32 nm, 0.5–0.6 nm, and 0.85 nm, respectively (Fig. 9). With the increasing of deformation T and P_c conditions, the PSDs of micropores display no significant changes, but the pore

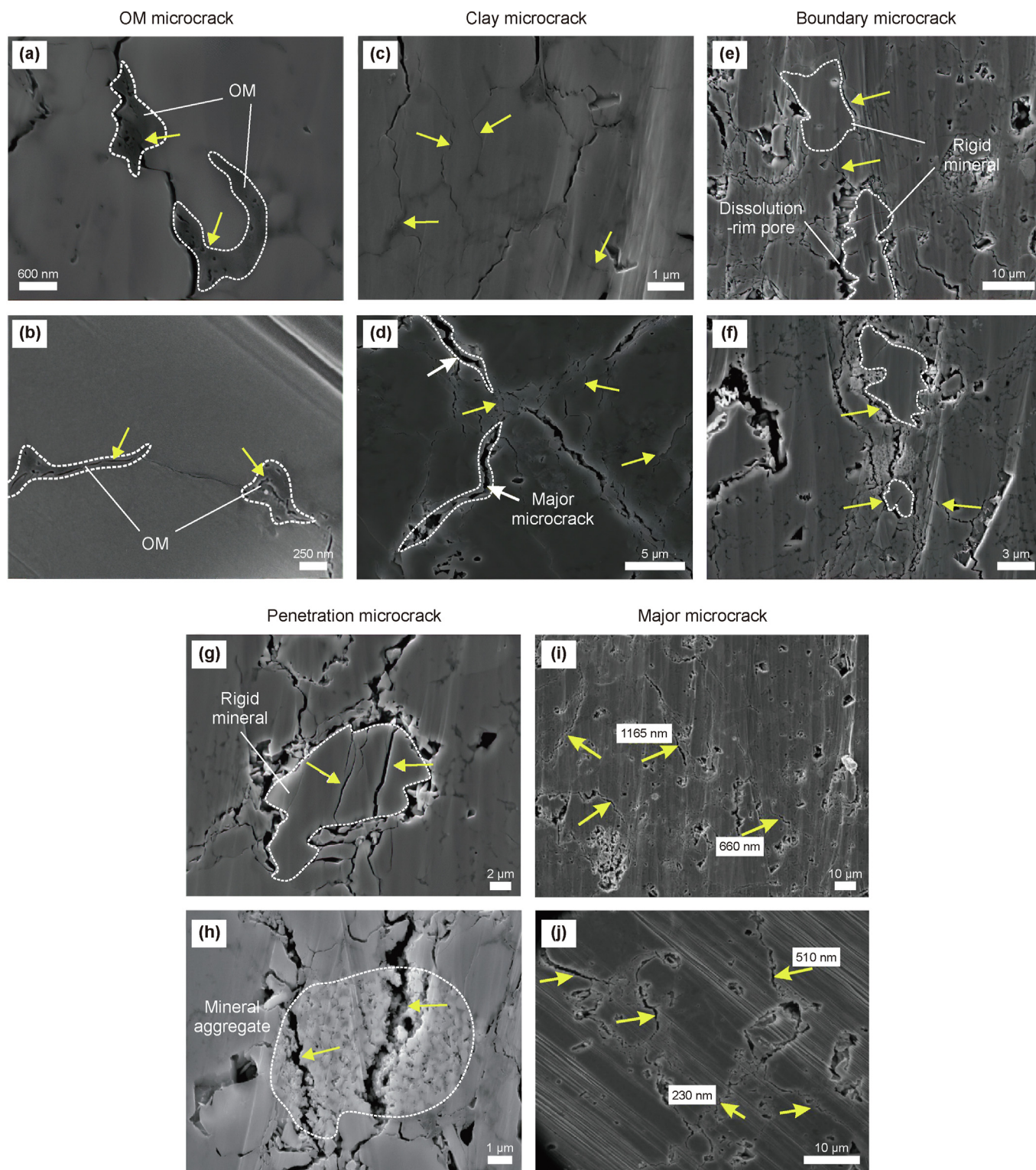


Fig. 7. Different microcracks identified in experimentally deformed shales. Yellow solid arrows represent corresponding types of microcracks.

volume overall display a downward trend from the brittle to ductile regime (Fig. 9). The decrease of mesopores as well as the increase of macropores might result from the interconnection of various previously isolated pores by microcracks generated during deformation. This explanation is also consistent with the microscopic observation of this study (Figs. 4–6) and some previous studies

based on natural samples (Liang et al., 2017; Zhu et al., 2018). The centralization of PSD during the brittle-ductile transitional and ductile deformation stage suggests that there might be a maximum for pore interconnection and microcrack extension, which can be reached when the vast majority of pores are interconnected.

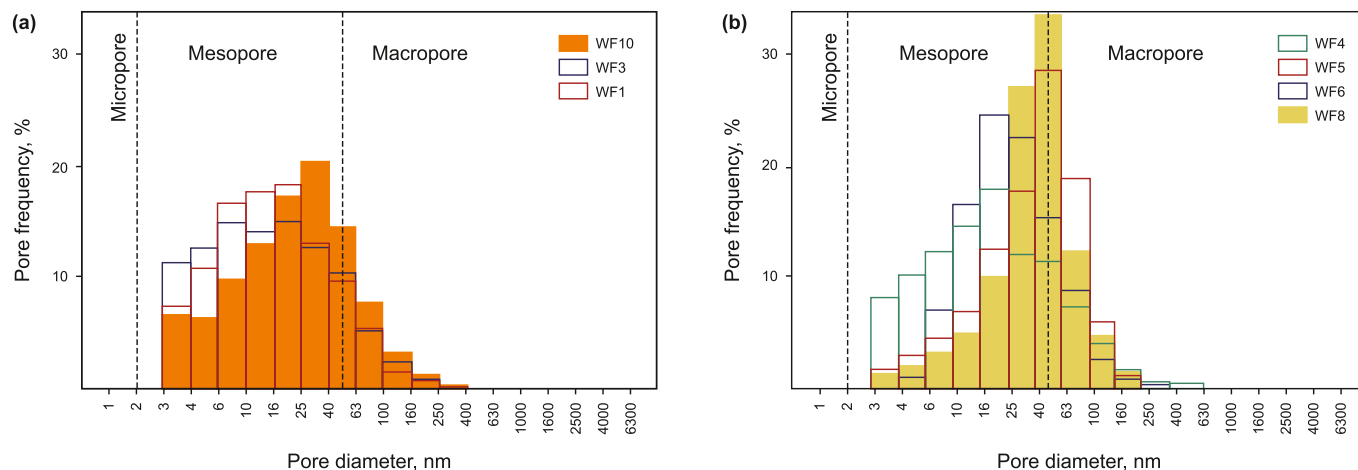


Fig. 8. Pore size distribution of (a) undeformed (WF10) and brittle-deformed shales (WF1, WF3); (b) brittle-ductile transitional (WF4, WF5, WF6) and ductile-deformed shales (WF8) identified by MIP.

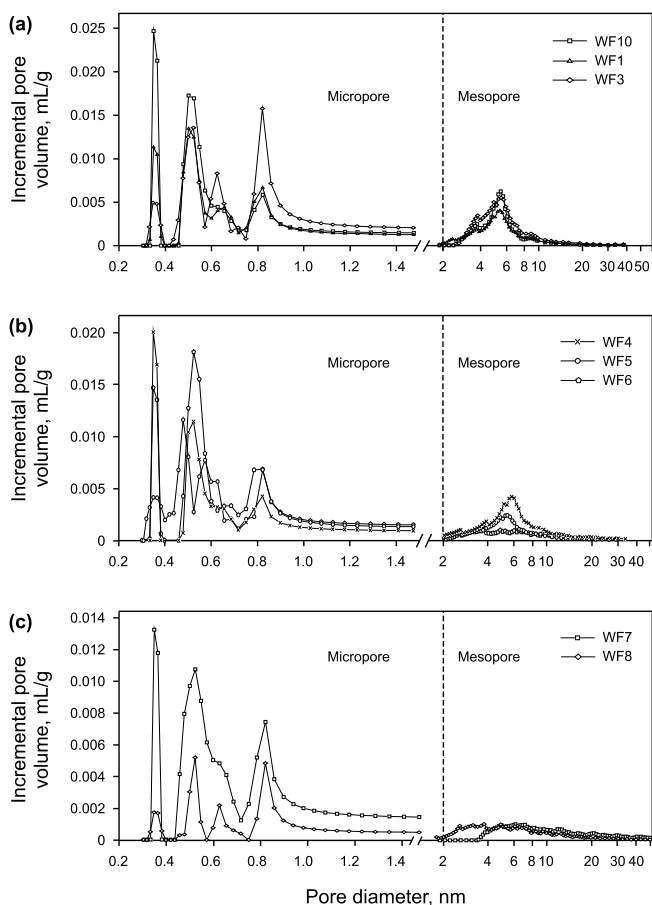


Fig. 9. Pore size distribution of (a) brittle-deformed shales (WF10, WF1, WF3); (b) brittle-ductile transitional deformed shales (WF4, WF5, WF6); and (c) ductile-deformed shales (WF7, WF8) defined by incremental pore volume using low-pressure gas adsorption analyses (N_2 and CO_2). Micropores are determined by CO_2 adsorption data, mesopores are from N_2 adsorption data. Dashed lines highlight the boundaries between micro- and mesopores.

3.4.2. Pore volume, specific surface area, and pore diameter (mode)

For further exploring the microstructure changes of shales, experimental data from low-temperature CO_2 and N_2 adsorption were used to calculate pore-structure-related parameters (pore

volume, SSA, and pore diameter (mode)) of micropores and mesopores, respectively (Fig. 10 and Table 2). From brittle to ductile deformation, except for WF7, the changes of micro- and mesopores display consistent trends in both pore volumes and SSAs (Fig. 10), indicating that OM and clay minerals provide the most micro- and mesopores as the positive correlation between their contents and SSA values have been reported by previous studies (Boruah et al., 2019; Ju et al., 2018; Kuila and Prasad, 2013; Tang et al., 2016). Pore diameter (mode) shows a stable distribution with a variation range less than 0.1 nm and 0.5 nm in mesopores and micropores, respectively, indicating the variation of pore volume and SSA is induced by changes in pore number rather than pore size (Fig. 10(c)). During the brittle deformation stage from WF10 to WF1, the volume of mesopores increases while that of micropores maintains stability first and then slightly decreases (Fig. 10(a), (b)), probably indicating that micropores within clays and OM are interconnected by microcracks in small areas to form mesopores, which is consistent with SEM observations in this study (Fig. 5(c) and 7(b)). Or, the compression of primary macropores to form mesopores might also be a causing factor in this case, which is consistent with the downward trend of macropores in Fig. 8(a).

During the brittle-ductile transitional and ductile stage from WF4 to WF8, the volume of mesopores conversely decreases while that of micropores increases significantly first and then decreases gradually (Fig. 10(a), (b)). Combined with the increasing trend of macropores during ductile deformation revealed by MIP analysis (Fig. 8), the decrease in mesopore volume can be explained by the propagation of microcracks further interconnecting various primary mesopores and forming pore networks, which is also in agreement with microscopic observations (Fig. 6). The significant rise of both pore volume and SSA of micropores at the beginning of brittle-ductile transitional stage indicates that the amount of micropores increases greatly, which might be the consequence of the plastic flow of soft matrix in shales. Previous studies have found that the plastic flow of OM and clay minerals would form a kind of OM-clay aggregate during ductile deformation, within which a great number of intergranular micropores can be generated or preserved between OM particles and clay mineral flakes (Ju et al., 2018; Ma et al., 2014; Macquaker et al., 2014; Zhu et al., 2018). In the present study, although no obvious flow structure has been found in the matrix of shales in this study due to the space limitation of the sample chamber, it is also reasonable to infer that some layered clay minerals formed micro-folds during ductile deformation, thus generating a certain number of intergranular

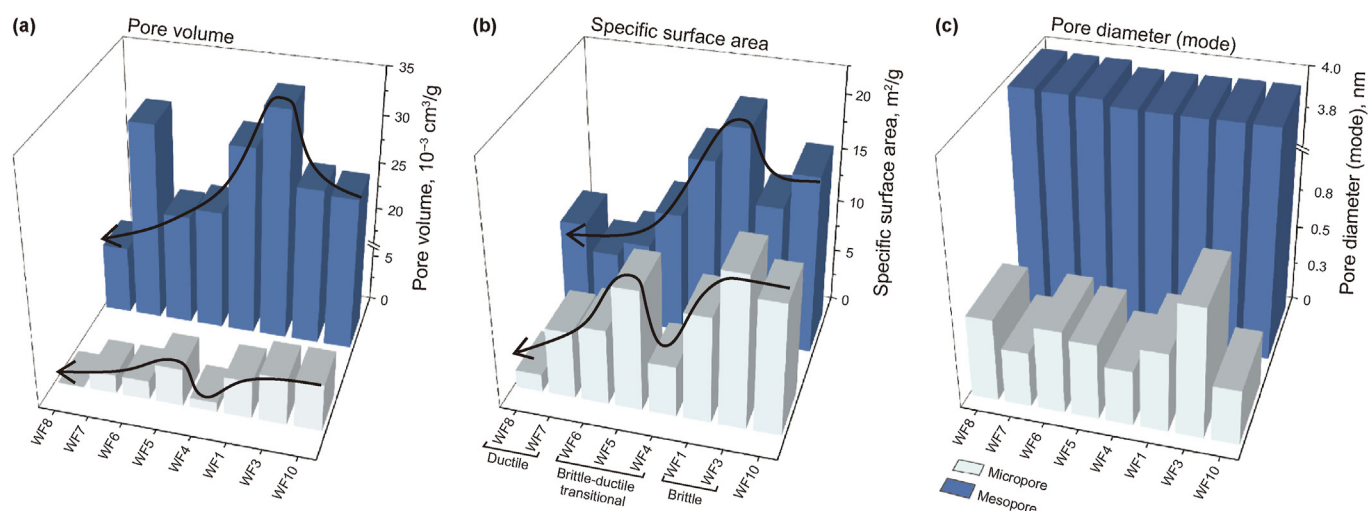


Fig. 10. The trend of changes in (a) micro- and mesopore volume; (b) specific surface areas of micro- and mesopores; and (c) pore diameters (mode) of micro- and mesopores in experimentally deformed shales. Mesopores and micropores are represented by N_2 absorption and CO_2 absorption data, respectively.

pores at the hinge zones of folded clays and accounting for the significant rebound of micropores volume.

3.5. Comparison between naturally and experimentally deformed shales

3.5.1. Pore size distribution in naturally and experimentally deformed shales

Before this study, a lot of previous studies have been conducted to reveal the influence of tectonic modification on pore-crack parameters of naturally deformed shales (Ju et al., 2018; Li et al., 2021; Liang et al., 2017; Zeng et al., 2023; Zhu et al., 2018, 2019). The results of these studies generally indicate that the number of macro- and mesopore would increase and the SSA and gas absorption capacity would decrease, while during the brittle-ductile transitional or ductile deformation, the SSA and gas absorption capacity would conversely increase accompanied by the increase of micropores. By comparison, the changes of pore-crack parameters along with the enhancement of deformation presented in this study are much more subtle with complex variation trend (Fig. 10). During the brittle deformation stage from WF10 to WF1, the volume of micropores remains relatively steady (Fig. 10(a)), which is consistent with results of natural sample research (Liang et al., 2017) and can be explained by the fact that small pores are generally more resistant to mechanical compaction (Katz and Arango, 2018; Loucks et al., 2009; Milliken and Curtis, 2016). However, different from the results of natural sample research, the proportion of macropores decreases (Fig. 8) while the pore volume of mesopores increases in this study (Fig. 10), of which reason might be the discrepancies between the experimental and natural deformation environment. As mentioned above, in a natural environment, shale deformation in the horizontal direction often has no displacement limitation, manifested by structures like faults, detachment, duplex, thrust nappe, etc. That are common in the field. Along with the formation of these structures, a large number of large pores and micro-fractures would develop within the shale layer, accounting for the rise of macropore proportion in naturally deformed shales as stated by Zhu et al. (2018, 2019), Ju et al. (2018), and Ma et al. (2020). In comparison, the experimental brittle-deformation process is more of compaction rather than shearing, thus being more inclined to cause the collapse and compression of primary macropores rather than generate fractures (Pommer and

Milliken, 2015; Yang and Aplin, 1998). Thus, the opposite trend of macro- and mesopores might result from the transformation between them.

In naturally deformed shales with rheological characteristics, the proportion of micropores as well as the SSA of shales is widely regarded as higher than conventional shales. Its microscopic genetic mechanism can be diverse. For example, some scholars argue that the compression of pores in ductile materials (OM and clay particles) can account for the increase in micropores (Guo et al., 2022b; Ma et al., 2015). Even though Desbois et al. (2009) and Loucks et al. (2012) argue that pores surrounded by ductile grains would be insusceptible to compaction or deformation due to the sheltering effect provided by surrounding rigid grains, the collapse and compression of this kind of pores have been verified by modeling (Singh et al., 2010) and microimaging of natural samples (Ma et al., 2015; Sun et al., 2023; Zeng et al., 2023). Besides, the “mylonitized structure”, within which the contact boundaries between OM particles and clay minerals can develop a great number of nanometer-size intergranular pores, is also considered a mechanism that can create micropores during ductile deformation (Ma et al., 2014; Zhu et al., 2018). In this study, micropore volume displays a “two-stage mode” of first ascending and then descending during the brittle-ductile transitional and ductile deformation stages from WF4 to WF8 (Fig. 10(a)), which seems to differ from naturally deformed samples mentioned above. We believe that this discrepancy is caused by differences in T and P_c conditions between natural and experimental deformation processes. As mentioned in the “Methodology” section, the deformation conditions of WF7 and WF8 were set far beyond the real geological background to explore the deformation behavior of shales within a larger range of T and P_c conditions. Taking the Fuling area as an example (location see Fig. 1), the maximum temperature of the Wufeng Formation and Longmaxi Formation there during their evolutionary processes is estimated to be around 200 °C (Nie et al., 2020), and the maximum pressure of them is estimated to be about 73.58–85.36 MPa (Jin and Nie, 2022). These P – T conditions are similar to WF4 ($T = 90$ °C, $P_c = 60$ MPa), WF5 ($T = 90$ °C, $P_c = 110$ MPa), and WF6 ($T = 200$ °C, $P_c = 110$ MPa). As discussed in Section 3.2, the P_c condition affects the deformation behavior more significantly than temperature does. Thus, the real deformation behavior under such maximum conditions ($T = 200$ °C, $P_c = 73.58$ – 85.36 MPa) is supposed to be similar to WF4 and WF5, which display increasing trend in both

micropore volume and SSA along with deformation enhancement. Therefore, the pore-crack structure changes of shale during the brittle-ductile deformation stage in this experiment are consistent with those of naturally deformed shale, indicating that this experiment has well simulated the natural deformation process of shale and its results are highly reliable. Concerning WF6, WF7, and WF8, they may represent examples that are deformed under ultrahigh T and P_c conditions, and both of their meso- and micropores generated by ductile deformation within clays or OM would greatly decrease under strong compression. Based on the results of this study, the T and P_c conditions at the turning point of shale porosity are about $T = 90\text{--}200\text{ }^\circ\text{C}$ and $P_c = 110\text{ MPa}$, respectively.

3.5.2. Permeability in naturally and experimentally deformed shales

Another important pore-crack parameter that shows differences between natural and experimentally deformed shale is permeability. Before this study, numerous studies have investigated the effect of brittle and ductile deformation on the permeability of not only shales but also other unconventional reservoir rocks like coals (Ju et al., 2018; Li et al., 2003; Needham, 2004; Sun et al., 2023; Zeng et al., 2023; Zhu et al., 2019). Nowadays, the permeability of shale and coal is commonly considered to decrease along with ductile deformation. For example, Li et al. (2003) found that non-connected cracks in ductile-deformed mylonitic coal show compressive features with low permeability; Sun et al. (2023) stated that the Niutitang Formation shale in deformed regions displays much lower pore connectivity in nano-CT images than that in stable regions. Apart from natural sample studies, shear tests in the laboratory also prove that shear fractures created in ductile shales have reduced permeability with increasing shear deformation (Gutierrez et al., 2000). The results of these studies are contrary to those of this study. Although no permeability data of experimentally deformed shales were collected in this study, the formation of various open microcracks and the interconnection of different pores observed in SEM images (Fig. 6), combined with the increase in the proportion of macropores (Fig. 8), undoubtedly can contribute to greater permeability.

Two possible reasons might account for this contradiction. The first is that deformation experiments are incapable of simulating widely existing fluid activities in geological processes. Zeng et al. (2023) and Zhu et al. (2018) suggested that the later tectonic compaction is not the only reason for the reduction of open cracks, calcite veins, transport asphaltene, and authigenic clay minerals grow or transported in these open cracks can also reduce the permeability of shale. Besides, Gutierrez et al. (2000) also stated that microcracks are unlikely to close under mechanical loading after formation even during ductile deformation, because fractures in tight formations like shales will always be conduits for fluid flow unless closed by cementation. However, it does not mean that open microcracks are impossible to exist in naturally ductile-deformed shales since ductile-deformed shales with high connectivity have also been found in the field (Zeng et al., 2023; Zhu et al., 2019), possibly indicating a deformation environment lacking fluid activity. The second possible reason might be the discrepancy in substance composition of different shales, which can largely affect the deformation behavior of shales under certain T and P_c conditions. In this study, we infer that the content of ductile material (i.e., clay and OM) is possibly a key factor affecting the permeability of deformed shales, especially during the ductile deformation stage. It is widely accepted that there is a close relationship between brittle grains (i.e., quartz, calcite, etc.) and fracturing during the brittle deformation stage of shales since the grain boundaries are weak structural surfaces where stress usually concentrates (Kranz, 1983). When the loading stress reaches a certain threshold, open microcracks would form to release local stress along these weak surfaces,

which can significantly increase the permeability (Fig. 11(a)). When transitioning to the ductile deformation stage with higher T and P_c conditions, if the content of ductile material is high enough, their plastic deformation would accommodate the displacement required for the later tectonic compaction, thus enabling microcracks to be preserved (Fig. 11(b)). Conversely, if the content of ductile material is low, since brittle materials are less prone to ductile deformation, previously formed open microcracks would be compressed to adjust to the compressive stress, thus resulting in the decline of shale permeability (Fig. 11(c)). This viewpoint is also verified by an experiment conducted by Olgaard et al. (1997), which proved that mudrocks with low clay content are stronger and more brittle than those with high clay content for a given effective pressure. However, as no control group with different mineral compositions was set up for compression experiments in this study, this inference still needs further verification.

3.6. Model of micro pore-crack system evolution in deformed shales

The micro pore-crack system in shale is formed by the interconnection among various pores and microcracks and is widely considered to have a significant impact on the storage and seepage ability of shale reservoirs. So far, most studies on it are based on natural shales with different deformation levels in different regions (Liu et al., 2019; Loucks et al., 2009, 2012; Ma et al., 2020; Slatt and O'Brien, 2011; Wang et al., 2019), making them hard to exclude the influence of factors such as rock composition, thermal evolution history, and tectonic history, thus further hindering the understanding of the continuous evolution process of micro pore-crack system. The present study, utilizing physical deformation simulation methods, can make up for the shortcomings in this area. From the SEM images of weakly deformed shales (WF1, WF3, WF4), the initial formation of the micro pore-crack system is observed to be related to rigid particles and primary pores. Firstly, the deterioration of cementation between clayey matrix and rigid particles gives rise to an unstable state of particle boundary areas (Fig. 5(b)), and then clay phyllosilicates may be squeezed into primary dissolution-rim pores, resulting in the change of pore morphology (Fig. 5(b)). As the level of deformation increases, microcracks gradually extend and expand. In WF8 with the strongest deformation, a complete micro pore-crack system is observed (Fig. 12(a)). As marked in Fig. 12(b)—a major microcrack originates from a dissolution-rim pore, and then divides into two branches downward, both of which cut through clays and OM, creating clay microcracks and organic-matter microcracks. Lower down to Fig. 12(c), the hindrance of rigid grains forces the stresses to extend along the particle edges or cut through particle bodies, forming boundary microcracks and penetration microcracks, which are subsequently suspended by connecting to another dissolution-rim pore below. Further down to Fig. 12(d)—a new cycle begins with stress continuing to propagate along rigid particle edges and within the clayey matrix, forming boundary microcracks and clay microcracks.

Combined with SEM imaging and results of pore-crack parameter tests, an ideal model of micro pore-crack system formation and evolution is proposed (Fig. 13). To start with, during the brittle deformation stage, microcracks begin to form by the collapse of weak primary pores (dissolution-rim pores, interparticle pores, etc.) (Fig. 13(a)) and extend outward along weak areas such as clay minerals or OM in the matrix, forming net-like and dispersed clay microcracks and organic-matter microcracks (Fig. 13(b)). During this process, some primary macropores that are not protected by rigid materials would be compressed, and some OM-hosted micropores and clay-hosted micropores would be connected by microcracks (Fig. 13(b)), resulting in an increase in mesoporous volume and a decrease in both macro- and microporous volume

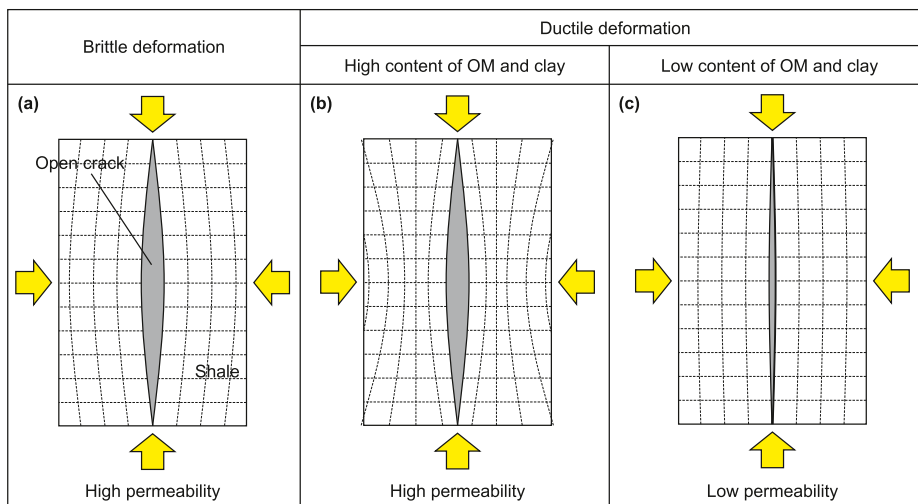


Fig. 11. Sketch of changes of shale permeability during (a) brittle deformation; (b) ductile deformation with low OM and clay content; and (c) ductile deformation with high OM and clay content.

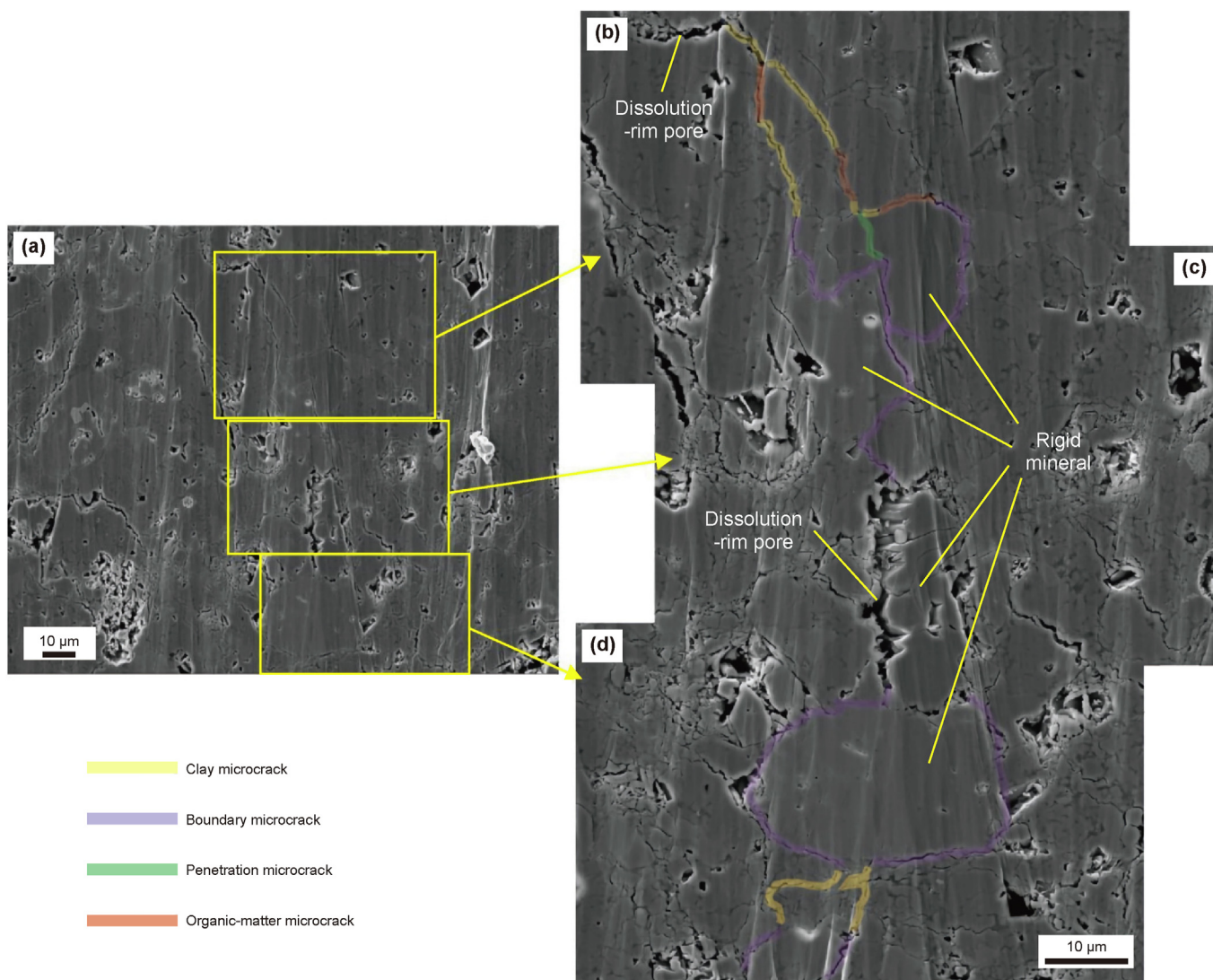


Fig. 12. SEM images of a typical micro pore-crack system developed in deformed shale (WF8).

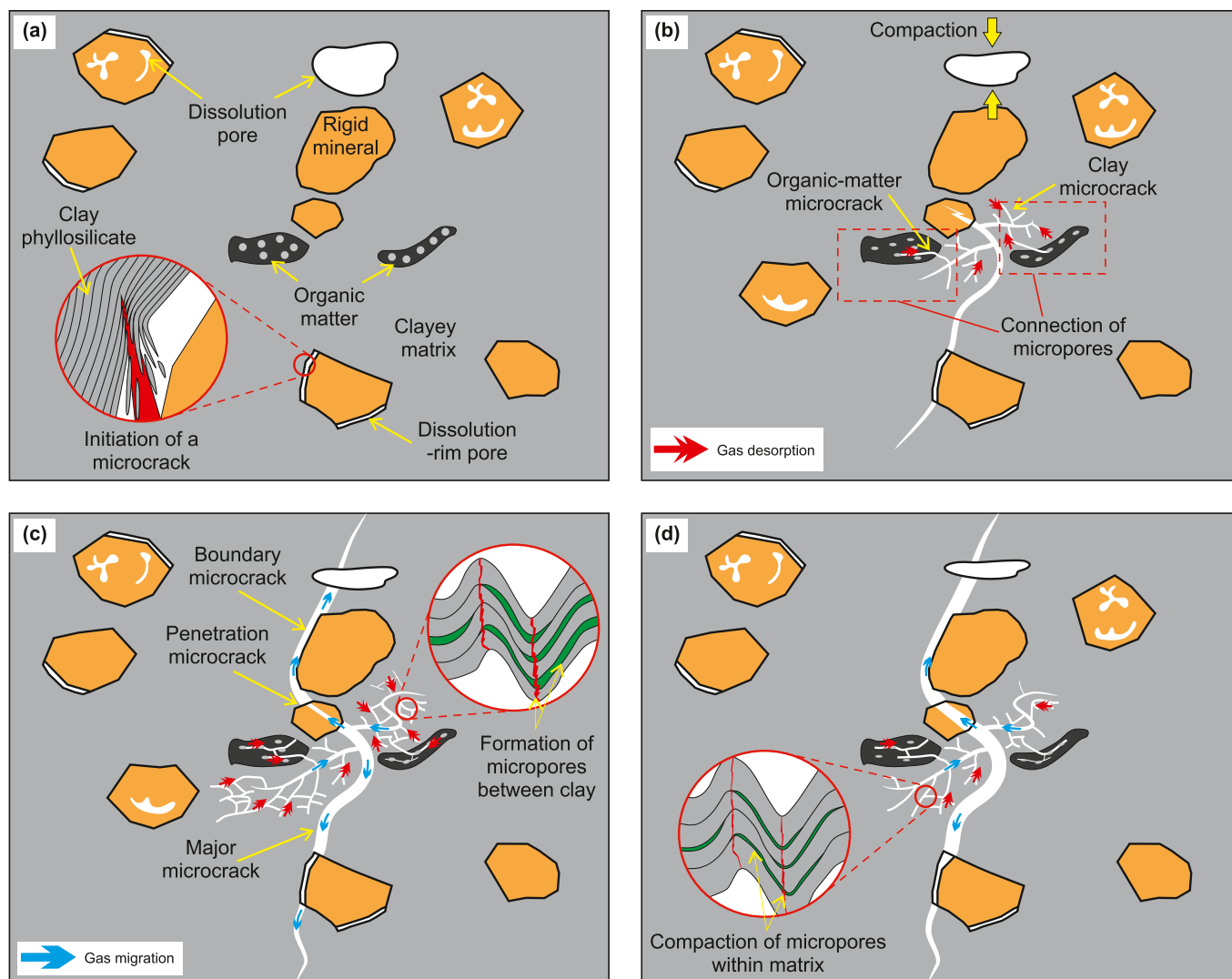


Fig. 13. Sketch of the formation and evolution of a micro pore-crack system in shale during (a, b) brittle deformation stage; (c) brittle-ductile transitional deformation stage; and (d) ductile deformation stage.

(Fig. 8(a) and 10(a)). The degree of development of primary pores as well as the content of brittle minerals might be controlling factors during this stage since they are all beneficial for the initiation and preliminary extension of microcracks.

Subsequently, during the brittle-ductile transitional deformation stage, microcracks would continue to extend and propagate, generating boundary microcracks when encountering small or hard particles, or generating penetration microcracks when encountering large or brittle particles as the development of boundary microcracks is insufficient to fully transmit the stress, finally terminating and being absorbed in another pore where a new cycle might initiate again (Fig. 13(c)). Along the path with the minimum stress required for fracturing, these microcracks would interconnect with each other to form major microcracks and interconnect various mesopores as well, leading to the increase of macropores and decrease of mesopores (Figs. 8 and 10(a)). Within the matrix, a series of clay-hosted micropores would be formed by plastic deformation (Fig. 13(c)), thereby causing the increase of micropore volume (Fig. 10(a)). Finally, during the ductile deformation stage, major microcracks would continue to extend and expand, while micropores hosted in the soft matrix would be intensively distorted and compacted by plastic deformation (Fig. 13(d)), leading to the

decline of both micro- and mesopores volume (Fig. 10(a)). In the last two stages, the contents of OM and clay have a significant impact on the pore-crack structure of shales, because by undergoing plastic deformation, they can not only produce a certain amount of micropores but also prevent microcracks from closing.

3.7. Implications for further exploration of shale gas

In recent years, with the development of the shale gas industry in China, the focus of shale gas exploration has gradually shifted from shallow to deep (burial depth of 3500–4500 m) and ultra-deep (burial depth greater than 4500 m) layers, and from structurally stable zones to structurally complex zones (Li et al., 2023; Ma et al., 2023). In terms of exploration theory, the mechanism of pore preservation in deep shale reservoirs, as well as the critical points and conditions of brittle-ductile transition in deep shale reservoirs and their impact on fracture development, are all crucial issues to be solved (Guo et al., 2022a).

Based on the results of this study, the range of T and P_c conditions for brittle deformation is confined to be $T < 50^\circ\text{C}$ and $P_c < 60\text{ MPa}$, while that of brittle-ductile transitional deformation is $90^\circ\text{C} < T < 200^\circ\text{C}$ and $60\text{ MPa} < P_c < 110\text{ MPa}$ and that of ductile

deformation is $T > 200$ °C and $P_c > 110$ MPa. Relative to temperature, the pressure is proved to be more effective in affecting the brittle-ductile transition. In the exploration process of deep shale gas, especially when the number of deep drilling samples is relatively limited, it is usually difficult to determine the deformation characteristics of deep shale. In this situation, by confining the T – P conditions for brittle-ductile transition and combining methods such as basin subsidence simulation and paleotectonic stress tests in field research, the deformation characteristics of deep shale can be determined.

Moreover, the present study also reveals the trend of changes in pore-crack structure especially under high T , P conditions, of which results indicate that both micro- and mesopores decrease dramatically at high pressure (>110 MPa) (Fig. 10(a)). This means that many previous studies have overestimated the growth of micropores in the process of ductile deformation. In fact, the increase in the number of micropores might only occur in the early stage of ductile deformation (also known as brittle-ductile deformation stage), and when the T – P conditions exceed a certain threshold, the number of micropores will significantly decrease. The results of natural sample research are also consistent with this viewpoint. For example, the Cambrian Niutitang Formation shale in the deformed region ($P_{\max} = 184$ MPa) has a lower microporous proportion than that in the stable region ($P_{\max} = 156$ MPa) (Sun et al., 2023). These pressure conditions are all within the ductile scope confined in this study, but the proportion of micropores does not increase with the enhancement of deformation, which is consistent with the conclusion of this study. Therefore, shales with brittle-ductile transitional deformation which possess both high proportions of micropores (adsorption capacity) and well-developed micro pore-crack systems (desorption and percolation capability) are suggested to be of great energy potential in the exploration and evaluation of shale gas resource.

Furthermore, the continuous enhancement of permeability caused by the development of micro pore-crack systems has implications for shale gas exploration as well, especially for ductile deformed shales. The micro pore-crack system, formed by the connection between pores and microcracks of different volumes and types, can provide a key foundation for the desorption, migration, and seepage of gas molecules (Fig. 13(d)), thus being beneficial for the development of shale gas. In this study, we suggest that open microcracks can be preserved during ductile deformation if the ductile material content in shale is high. This viewpoint can be applied in the field works. For example, when exploring deep and ancient ductile deformed shale layers, the content of clay and OM in them can be used as one of the parameters to predict their permeability. Although these microcracks may be filled and cemented to form veins during later fluid activities, leading to a decrease in permeability, the tensile strength of the contact between veins and the surrounding rock is usually very low, making them easily destroyed during hydraulic stimulation (Gale et al., 2007; Zhu et al., 2018). Excluding its effect on microcrack preservation, ductile materials (OM and clay) are widely considered to possess massive adsorption sites for shale gas (Han et al., 2016; Ross and Bustin, 2009; Wang et al., 2015a). Therefore, the ductile material content should be given more attention in future exploration.

4. Conclusions

- (1) The physical deformation simulation of shale indicates that the experimental brittle deformation of shales happens under conditions of $T < 90$ °C and $P < 60$ MPa, and the brittle-

ductile transitional deformation happens under conditions of 90 °C $< T < 200$ °C and 60 MPa $< P < 110$ MPa, while the ductile deformation occurs at $T > 200$ °C and $P > 110$ MPa. Temperature can significantly affect the mechanical behavior of shales and reduce their peak strength only when the P_c is low, while pressure, which can raise the peak strength of shales and promote their brittle-ductile transition, is the dominant factor under high P_c conditions;

- (2) During brittle deformation of shales, the volume of mesopores increases while that of micro- and macropores decreases due to the compaction of primary pores and the interconnection of OM- and clay-hosted micropores. During the brittle-ductile transitional deformation, the volume of mesopores decreases while that of micro- and macropores increases because of the further interconnection among mesopores by microcracks and the new formation of micropores by ductile deformation within the clayey matrix. During ductile deformation, the volume of both micro- and mesopores decreases while that of macropores increases. This is because those previously formed microcracks would continue to expand and connect various pores under loading, while micropores formed within the clayey matrix are damaged by late over-intense compression. The ductile material (i.e., clay and OM) content in shales might be a key factor determining whether open microcracks can be preserved after ductile deformation;
- (3) Based on SEM observations, an ideal model of micro pore-crack system formation and evolution is proposed: Under stress, microcracks initiate from the collapse of a primary pore, and then extend along weak areas (i.e., clay minerals and OM) to form net-like clay microcracks and organic-matter microcracks; with the stress increasing, boundary microcracks and penetration microcracks generate along potential cracking planes near or within rigid minerals; when encountering with another pre-existing pore, microcracks would terminate and a new cycle might initiate again. The understanding of changes in pore-crack parameters as well as the formation and evolution of micro pore-crack systems along with deformation enhancement in shales is of great significance for further shale gas exploration, especially for deep shales and shales in structurally complex zones.

CRediT authorship contribution statement

Yi-Wen Ju: Supervision, Funding acquisition, Conceptualization. **Xin-Gao Hou:** Writing – review & editing, Writing – original draft, Visualization. **Kui Han:** Writing – original draft, Methodology, Investigation. **Yu Song:** Data curation. **Lei Xiao:** Data curation. **Cheng Huang:** Data curation. **Hong-jian Zhu:** Data curation. **Li-Ru Tao:** Data curation.

Declaration of competing interest

The authors declare the following financial interests/personal relationships which may be considered as potential competing interests:

Yiwen Ju reports financial support was provided by National Natural Science Foundation of China. If there are other authors, they declare that they have no known competing financial interests or personal relationships that could have appeared to influence the work reported in this paper.

Acknowledgments

We gratefully acknowledge the anonymous reviewers for their constructive comments which much improved the manuscript. The authors would like to show their gratitude to Chang-Rong He and Lei Zhang for their help with the triaxial compression test, and to all the researchers who assisted in our work. This work was supported by the National Natural Science Foundation of China (Grant Nos. 42372153, 41530315); the National Key Research and Development Program of China (Grant No. 2023YFF0804300); the National Science and Technology Major Project of China (Grant Nos. 2016ZX050066, 2017ZX05064); and the “Climate Change: Carbon Budget and Related Issues” Strategic Priority Research Program of the Chinese Academy of Sciences (Grant No. XDA05030100).

Abbreviations

T	temperature
P	pressure
P _c	confining pressure
PSD	pore size distribution
SSA	specific surface area
TOC	total organic carbon
SEM	scanning electron microscopy
OM	organic matter
MIP	mercury intrusion porosimetry

References

- Antonellini, M.A., Aydin, A., Pollard, D.D., 1994. Microstructure of deformation bands in porous sandstones at Arches National Park, Utah. *J. Struct. Geol.* 16 (7), 941–959. [https://doi.org/10.1016/0191-8141\(94\)90077-9](https://doi.org/10.1016/0191-8141(94)90077-9).
- Aydin, M.G., Engelder, T., 2014. Revisiting the Hubbert-Rubey pore pressure model for overthrust faulting: inferences from bedding-parallel detachment surfaces within Middle Devonian gas shale, the Appalachian Basin, USA. *J. Struct. Geol.* 69, 519–537. <https://doi.org/10.1016/j.jsg.2014.07.010>.
- Boruah, A., Rasheed, A., Mendhe, V.A., Ganapathi, S., 2019. Specific surface area and pore size distribution in gas shales of Raniganj Basin, India. *J. Pet. Explor. Prod. Technol.* 9 (2), 1041–1050. <https://doi.org/10.1007/s13202-018-0583-8>.
- Bowker, K.A., 2007. Barnett shale gas production, fort worth basin: issues and discussion. *AAPG Bull.* 91 (4), 523–533. <https://doi.org/10.1306/06190606018>.
- Bustin, R.M., Bustin, A.M.M., Cui, X., Ross, D.J.K., Pathi, V.S.M., 2008. Impact of shale properties on pore structure and storage characteristics. *One Petro.* <https://doi.org/10.2118/119892-MS>.
- Cao, H., Zhu, C., Qiu, N., 2015. Thermal evolution of lower silurian Longmaxi Formation in the eastern Sichuan Basin. *J. Earth Sci. Environ.* 37 (6), 22–32. <https://doi.org/10.3969/j.issn.1672-6561.2015.06.003> (in Chinese).
- Chalmers, G.R., Bustin, R.M., Power, I.M., 2012. Characterization of gas shale pore systems by porosimetry, pycnometry, surface area, and field emission scanning electron microscopy/transmission electron microscopy image analyses: examples from the Barnett, Woodford, Haynesville, Marcellus, and Doig units. *AAPG Bull.* 96 (6), 1099–1119. <https://doi.org/10.1306/10171111052>.
- Cheng, G., Jiang, B., Li, F., Li, M., Song, Y., Hou, C., 2023. Experimental study on brittle-to-ductile transition mechanism of lower Silurian organic-rich shale in south China. *Int. J. Rock Mech. Min. Sci.* 170, 105543. <https://doi.org/10.1016/j.ijrmm.2023.105543>.
- Desbois, G., Urai, J., Kukla, P., 2009. Morphology of the pore space in claystones – evidence from BIB/FIB ion beam sectioning and cryo-SEM observations. *eEarth Discuss.* 4, 1–19. <https://doi.org/10.5194/eed-4-1-2009>.
- Eberhardt, E., Stead, D., Stimpson, B., Read, R.S., 1998. Identifying crack initiation and propagation thresholds in brittle rock. *Can. Geotech. J.* 35 (2), 222–233. <https://doi.org/10.1139/t97-091>.
- Eichhubl, P., D’Onfro, P.S., Aydin, A., Waters, J., McCarty, D.K., 2005. Structure, petrophysics, and diagenesis of shale entrained along a normal fault at Black Diamond Mines, California—implications for fault seal. *AAPG Bull.* 89 (9), 1113–1137. <https://doi.org/10.1306/04220504099>.
- Erickson, S.G., 1994. Deformation of shale and dolomite in the Lewis thrust fault zone, northwest Montana, U.S.A. *Can. J. Earth Sci.* 31 (9), 1440–1448. <https://doi.org/10.1139/e94-127>.
- Eseme, E., Krooss, B.M., Littke, R., 2012. Evolution of petrophysical properties of oil shales during high-temperature compaction tests: Implications for petroleum expulsion. *Mar. Petrol. Geol.* 31 (1), 110–124. <https://doi.org/10.1016/j.marpetgeo.2011.11.005>.
- Gale, J.F.W., Reed, R.M., Holder, J., 2007. Natural fractures in the Barnett Shale and their importance for hydraulic fracture treatments. *AAPG Bull.* 91 (4), 603–622. <https://doi.org/10.1306/11010606061>.
- Gan, H., Nandi, S.P., Walker, P.L., 1972. Nature of the porosity in American coals. *Fuel* 51 (4), 272–277. [https://doi.org/10.1016/0016-2361\(72\)90003-8](https://doi.org/10.1016/0016-2361(72)90003-8).
- Gasparrini, M., Sassi, W., Gale, J.F.W., 2014. Natural sealed fractures in mudrocks: A case study tied to burial history from the Barnett Shale, Fort Worth Basin, Texas, USA. *Mar. Petrol. Geol.* 55, 122–141. <https://doi.org/10.1016/j.marpetgeo.2013.12.006>.
- Gregg, S.J., Sing, K.S.W., 1982. *Adsorption, Surface Area, and Porosity*. Academic Press, New York.
- Guo, T., 2016. Key geological issues and main controls on accumulation and enrichment of Chinese shale gas. *Petroleum Explor. Dev.* 43 (3), 349–359. [https://doi.org/10.1016/S1876-3804\(16\)30042-8](https://doi.org/10.1016/S1876-3804(16)30042-8).
- Guo, W., Guo, Y., Cai, Z., Yang, H., Wang, L., Yang, C., Zhao, G., Bi, Z., 2023. Mechanical behavior and constitutive model of shale under real-time high temperature and high stress conditions. *J. Pet. Explor. Prod. Technol.* 13 (3), 827–841. <https://doi.org/10.1007/s13202-022-01580-4>.
- Guo, X., Zhao, Y., Shen, B., Wei, X., Lu, L., Pan, A., Li, Y., 2022a. Marine shale gas exploration theory in southern China: Review and prospects. *Acta Geol. Sin.* 96 (1), 172–182. <https://doi.org/10.19762/j.cnki.dizhixuebao.2022271> (in Chinese).
- Guo, X., Liu, R., Xu, S., Feng, B., Wen, T., Zhang, T., 2022b. Structural deformation of shale pores in the fold-thrust belt: The Wufeng-Longmaxi shale in the Anchang Syncline of Central Yangtze Block. *Adv. Geo-Energy Res.* 6 (6), 515–530. <https://doi.org/10.46690/ager.2022.06.08>.
- Gutierrez, M., Øino, L.E., Nygård, R., 2000. Stress-dependent permeability of a de-mineralised fracture in shale. *Mar. Petrol. Geol.* 17 (8), 895–907. [https://doi.org/10.1016/S0264-8172\(00\)00027-1](https://doi.org/10.1016/S0264-8172(00)00027-1).
- Han, K., Ju, Y., Wang, G., Bao, S., Bu, H., Neupane, B., 2016. Shale composition and pore structure variations in the progradation direction: A case study of transitional shales in the Xu-Huai district, southern North China. *J. Nat. Gas Sci. Eng.* 36 (part B), 1178–1187. <https://doi.org/10.1016/j.jngse.2016.03.022>.
- He, C., Yao, W., Wang, Z., Zhou, Y., 2006. Strength and stability of frictional sliding of gabbro gouge at elevated temperatures. *Tectonophysics* 427 (1), 217–229. <https://doi.org/10.1016/j.tecto.2006.05.023>.
- Heath, J.E., Dewers, T.A., McPherson, B.J.O.L., Petrusak, R., Chidsey Jr., T.C., Rinehart, A.J., Mozley, P.S., 2011. Pore networks in continental and marine mudstones: Characteristics and controls on sealing behavior. *Geosphere* 7 (2), 429–454. <https://doi.org/10.1130/GES00619.1>.
- Herrmann, J., Rybacki, E., Sone, H., Dresen, G., 2018. Deformation experiments on Bowland and Posidonia Shale—Part I: Strength and Young’s modulus at ambient and in situ P_c-T conditions. *Rock Mech. Rock Eng.* 51 (12), 3645–3666. <https://doi.org/10.1007/s00603-018-1572-4>.
- Hillier, S., 1999. Use of an air brush to spray dry samples for X-ray powder diffraction. *Clay Min.* 34 (1), 127–135. <https://doi.org/10.1180/000985599545984>.
- Ibanez, W.D., Kronenberg, A.K., 1993. Experimental deformation of shale: Mechanical properties and microstructural indicators of mechanisms. *Int. J. Rock Mech. Min. Sci.* 30 (7), 723–734. [https://doi.org/10.1016/0148-9062\(93\)90014-5](https://doi.org/10.1016/0148-9062(93)90014-5).
- Jin, Z., Nie, H., 2022. Evolution history of overpressured and normally pressured shale gas reservoirs in Wufeng Formation–Longmaxi Formation, Sichuan Basin, China: An analysis from the perspective of source and seal coupling mechanism. *Energy Fuels* 36 (18), 10870–10885. <https://doi.org/10.1021/acs.energyfuels.2c01925>.
- Ju, Y., Sun, Y., Tan, J., Bu, H., Han, K., Li, X., Fang, L., 2018. The composition, pore structure characterization and deformation mechanism of coal-bearing shales from tectonically altered coalfields in eastern China. *Fuel* 234, 626–642. <https://doi.org/10.1016/j.fuel.2018.06.116>.
- Katz, B.J., Arango, I., 2018. Organic porosity: A geochemist’s view of the current state of understanding. *Org. Geochem.* 123, 1–16. <https://doi.org/10.1016/j.orggeochem.2018.05.015>.
- Klaver, J., Desbois, G., Urai, J.L., Littke, R., 2012. BIB-SEM study of the pore space morphology in early mature Posidonia Shale from the Hils area, Germany. *Int. J. Coal Geol.* 103, 12–25. <https://doi.org/10.1016/j.coal.2012.06.012>.
- Kranz, R.L., 1983. Microcracks in rocks: A review. *Tectonophysics* 100 (1), 449–480. [https://doi.org/10.1016/0040-1951\(83\)90198-1](https://doi.org/10.1016/0040-1951(83)90198-1).
- Kulla, U., Prasad, M., 2013. Specific surface area and pore-size distribution in clays and shales. *Geophys. Prospect.* 61 (2), 341–362. <https://doi.org/10.1111/1365-2478.12028>.
- Lei, W., Liu, X., Ding, Y., Xiong, J., Liang, L., 2023. The investigation on shale mechanical characteristics and brittleness evaluation. *Sci. Rep.* 13 (1), 22936. <https://doi.org/10.1038/s41598-023-49934-0>.
- Li, H., Ogawa, Y., Shimada, S., 2003. Mechanism of methane flow through sheared coals and its role on methane recovery. *Fuel* 82 (10), 1271–1279. [https://doi.org/10.1016/S0016-2361\(03\)00020-6](https://doi.org/10.1016/S0016-2361(03)00020-6).
- Li, M., Liu, Y., Feng, D., Shen, B., Du, W., Wang, P., 2023. Potential and future exploration direction of marine shale gas resources in China. *Petroleum Geology & Experiment* 45 (6), 1097–1108. <https://doi.org/10.11781/sydz2023061097> (in Chinese).
- Li, X., Zhu, H., Zhang, K., Li, Z., Yu, Y., Feng, X., Wang, Z., 2021. Pore characteristics and pore structure deformation evolution of ductile deformed shales in the Wufeng-Longmaxi Formation, southern China. *Mar. Petrol. Geol.* 127, 104992. <https://doi.org/10.1016/j.marpetgeo.2021.104992>.
- Liang, M., Wang, Z., Gao, L., Li, C., Li, H., 2017. Evolution of pore structure in gas shale related to structural deformation. *Fuel* 197, 310–319. <https://doi.org/10.1016/j.fuel.2017.02.035>.
- Liu, R., Hao, F., Engelder, T., Shu, Z., Yi, J., Xu, S., Teng, C., 2019. Stress memory

- extracted from shale in the vicinity of a fault zone: Implications for shale-gas retention. *Mar. Petrol. Geol.* 102, 340–349. <https://doi.org/10.1016/j.marpetgeo.2018.12.047>.
- Liu, Y., Liu, S., Liu, A., Kang, Y., 2022. Determination of mechanical property evolutions of shales by nanoindentation and high-pressure CO₂ and water treatments: A nano-to-micron scale experimental study. *Rock Mech. Rock Eng.* 55 (12), 7629–7655. <https://doi.org/10.1007/s00603-022-03059-4>.
- Loucks, R.G., Reed, R.M., Ruppel, S.C., Jarvie, D.M., 2009. Morphology, genesis, and distribution of nanometer-scale pores in siliceous mudstones of the Mississippian Barnett Shale. *J. Sediment. Res.* 79 (12), 848–861. <https://doi.org/10.2110/jsr.2009.092>.
- Loucks, R.G., Reed, R.M., Ruppel, S.C., Hammes, U., 2012. Spectrum of pore types and networks in mudrocks and a descriptive classification for matrix-related mudrock pores. *AAPG Bull.* 96 (6), 1071–1098. <https://doi.org/10.1306/08171111061>.
- Ma, X., Zhang, X., Xiong, W., Liu, Y., Gao, J., Yu, R., Sun, Y., Wu, J., Kang, L., Zhao, S., 2023. Prospects and challenges of shale gas development in China. *Petroleum Science Bulletin* 8 (4), 491–501. <https://doi.org/10.3969/j.issn.2096-1693.2023.04.037> (in Chinese).
- Ma, Y., Zhong, N., Han, H., Li, D., Zhang, Y., Cheng, L., 2014. Definition and structure characteristics of pores in mylonitized organic-rich shales. *Sci. China-Earth Sci.* 57 (12), 3027–3034. <https://doi.org/10.1007/s11430-014-4968-3>.
- Ma, Y., Zhong, N., Li, D., Pan, Z., Cheng, L., Liu, K., 2015. Organic matter/clay mineral intergranular pores in the Lower Cambrian Lujiaoping Shale in the north-eastern part of the upper Yangtze area, China: A possible microscopic mechanism for gas preservation. *Int. J. Coal Geol.* 137, 38–54. <https://doi.org/10.1016/j.coal.2014.11.001>.
- Ma, Y., Ardakani, O.H., Zhong, N., Liu, H., Huang, H., Larter, S., Zhang, C., 2020. Possible pore structure deformation effects on the shale gas enrichment: An example from the Lower Cambrian shales of the Eastern Upper Yangtze Platform, South China. *Int. J. Coal Geol.* 217, 103349. <https://doi.org/10.1016/j.coal.2019.103349>.
- Macquaker, J.H.S., Taylor, K.G., Keller, M., Polya, D., 2014. Compositional controls on early diagenetic pathways in fine-grained sedimentary rocks: Implications for predicting unconventional reservoir attributes of mudstones. *AAPG Bull.* 98 (3), 587–603. <https://doi.org/10.1306/08201311176>.
- Mastalerz, M., Schimmelmann, A., Drobnik, A., Chen, Y., 2013. Porosity of Devonian and Mississippian New Albany Shale across a maturation gradient: Insights from organic petrology, gas adsorption, and mercury intrusion. *AAPG Bull.* 97 (10), 1621–1643. <https://doi.org/10.1306/04011312194>.
- Milliken, K.L., Curtis, M.E., 2016. Imaging pores in sedimentary rocks: Foundation of porosity prediction. *Mar. Petrol. Geol.* 73, 590–608. <https://doi.org/10.1016/j.marpetgeo.2016.03.020>.
- Needham, T., 2004. Deformation in Moffat Shale detachment zones in the western part of the Scottish Southern Uplands. *Geol. Mag.* 141 (4), 441–453. <https://doi.org/10.1017/S0016756804009203>.
- Nie, H., He, Z., Wang, R., Zhang, G., Chen, Q., Li, D., Lu, Z., Sun, C., 2020. Temperature and origin of fluid inclusions in shale veins of Wufeng–Longmaxi Formations, Sichuan Basin, south China: Implications for shale gas preservation and enrichment. *J. Pet. Sci. Eng.* 193, 107329. <https://doi.org/10.1016/j.petrol.2020.107329>.
- Olgaard, D.L., Urai, J., Dell'Angelo, L.N., Nüesch, R., Ingram, G., 1997. The influence of swelling clays on the deformation of mudrocks. *Int. J. Rock Mech. Min. Sci.* 34 (3–4), 235e1–235e15. [https://doi.org/10.1016/S1365-1609\(97\)00182-2](https://doi.org/10.1016/S1365-1609(97)00182-2).
- Paterson, M.S., 1990. Rock deformation experimentation. In: Duba, A.G., Durham, W.B., Handin, J.W., Wang, H.F. (Eds.), *The Brittle-Ductile Transition in Rocks, the American Geophysical Union, Washington, D.C.*, pp. 187–194.
- Pommer, M., Milliken, K., 2015. Pore types and pore-size distributions across thermal maturity, Eagle Ford Formation, southern Texas. *AAPG Bull.* 99 (9), 1713–1744. <https://doi.org/10.1306/03051514151>.
- Ross, D.J.K., Bustin, R.M., 2009. The importance of shale composition and pore structure upon gas storage potential of shale gas reservoirs. *Mar. Petrol. Geol.* 26 (6), 916–927. <https://doi.org/10.1016/j.marpetgeo.2008.06.004>.
- Rybacki, E., Reinicke, A., Meier, T., Makasi, M., Dresen, G., 2015. What controls the mechanical properties of shale rocks? – Part I: Strength and Young's modulus. *J. Pet. Sci. Eng.* 135, 702–722. <https://doi.org/10.1016/j.petrol.2015.10.028>.
- Rybacki, E., Meier, T., Dresen, G., 2016. What controls the mechanical properties of shale rocks? – Part II: Brittleness. *J. Pet. Sci. Eng.* 144, 39–58. <https://doi.org/10.1016/j.petrol.2016.02.022>.
- Schieber, J., Krinsley, D., Riciputi, L., 2000. Diagenetic origin of quartz silt in mudstones and implications for silica cycling. *Nature* 406 (6799), 981–985. <https://doi.org/10.1038/35023143>.
- Schulmann, K., Mlčoch, B., Melka, R., 1996. High-temperature microstructures and rheology of deformed granite, Erzgebirge, Bohemian Massif. *J. Struct. Geol.* 18 (6), 719–733. [https://doi.org/10.1016/S0191-8141\(96\)80007-1](https://doi.org/10.1016/S0191-8141(96)80007-1).
- Setiawan, N.B., Zimmerman, R.W., 2018. Wellbore breakout prediction in transversely isotropic rocks using true-triaxial failure criteria. *Int. J. Rock Mech. Min. Sci.* 112, 313–322. <https://doi.org/10.1016/j.ijrmms.2018.10.033>.
- Sheng, M., Li, G., Huang, Z., Tian, S., Qu, H., 2013. Experimental study on hydraulic isolation mechanism during hydra-jet fracturing. *Exp. Therm. Fluid Sci.* 44, 722–726. <https://doi.org/10.1016/j.expthermflusc.2012.09.014>.
- Singh, R., Lee, P.D., Lindley, T.C., Kohlhauser, C., Hellmich, C., Bram, M., Imwinkelried, T., Dashwood, R.J., 2010. Characterization of the deformation behavior of intermediate porosity interconnected Ti foams using micro-computed tomography and direct finite element modeling. *Acta Biomater.* 6 (6), 2342–2351. <https://doi.org/10.1016/j.actbio.2009.11.032>.
- Slatt, R.M., O'Brien, N.R., 2011. Pore types in the Barnett and Woodford gas shales: Contribution to understanding gas storage and migration pathways in fine-grained rocks. *AAPG Bull.* 95 (12), 2017–2030. <https://doi.org/10.1306/03301110145>.
- Stocker, R.L., Ashby, M.F., 1973. On the rheology of the upper mantle. *Rev. Geophys.* 11 (2), 391–426. <https://doi.org/10.1029/RG011i002p00391>.
- Sun, C., Nie, H., Xiong, L., Du, W., Zhang, G., Chen, Q., Li, D., 2022. Main geological factors of enrichment and high yield of deep shale gas reservoirs in Weiyuan area, Sichuan Basin: Analyzed from the perspective of source-cap controlling hydrocarbon. *Marine Origin Petroleum Geology* 27 (2), 135–145. <https://doi.org/10.3969/j.issn.1672-9854.2022.02.003> (in Chinese).
- Sun, W., Zuo, Y., Lin, Z., Wu, Z., Liu, H., Lin, J., Chen, B., Chen, Q., Pan, C., Lan, B., Liu, S., 2023. Impact of tectonic deformation on shale pore structure using adsorption experiments and 3D digital core observation: A case study of the Niutitang Formation in Northern Guizhou. *Energy* 278, 127724. <https://doi.org/10.1016/j.energy.2023.127724>.
- Tan, J., Weniger, P., Krooss, B., Merkel, A., Horsfield, B., Zhang, J., Boreham, C.J., Graas, G.v., Tocher, B.A., 2014. Shale gas potential of the major marine shale formations in the Upper Yangtze Platform, South China, Part II: Methane sorption capacity. *Fuel* 129, 204–218. <https://doi.org/10.1016/j.fuel.2014.03.064>.
- Tang, H.M., Wang, J.J., Zhang, L.H., Guo, J.J., Chen, H.X., Liu, J., Pang, M., Feng, Y.T., 2016. Testing method and controlling factors of specific surface area of shales. *J. Pet. Sci. Eng.* 143, 1–7. <https://doi.org/10.1016/j.petrol.2016.02.009>.
- Uehara, S.I., Takahashi, M., 2014. Evolution of permeability and microstructure of experimentally-created shear zones in Neogene siliceous mudstones from Honobe, Japan. *J. Struct. Geol.* 60, 46–54. <https://doi.org/10.1016/j.jsg.2013.12.003>.
- Wang, F.P., Reed, R.M., John, A., Katherine, G., 2009. Pore networks and fluid flow in gas shales. *One Petro.* <https://doi.org/10.2118/124253-MS>.
- Wang, G., Ju, Y., Han, K., 2015a. Early Paleozoic shale properties and gas potential evaluation in Xiuwu Basin, western Lower Yangtze Platform. *J. Nat. Gas Sci. Eng.* 22, 489–497. <https://doi.org/10.1016/j.jngse.2014.12.025>.
- Wang, G., Ju, Y., 2015. Organic shale micropore and mesopore structure characterization by ultra-low pressure N₂ physisorption: Experimental procedure and interpretation model. *J. Nat. Gas Sci. Eng.* 27, 452–465. <https://doi.org/10.1016/j.jngse.2015.08.003>.
- Wang, G., Ju, Y., Yan, Z., Li, Q., 2015b. Pore structure characteristics of coal-bearing shale using fluid invasion methods: A case study in the Huainan-HuaiBei Coalfield in China. *Mar. Petrol. Geol.* 62, 1–13. <https://doi.org/10.1016/j.marpetgeo.2015.01.001>.
- Wang, Y., Li, C.H., Hao, J., Zhou, R.Q., 2018. X-ray micro-tomography for investigation of meso-structural changes and crack evolution in Longmaxi formation shale during compressive deformation. *J. Pet. Sci. Eng.* 164, 278–288. <https://doi.org/10.1016/j.petrol.2018.01.079>.
- Wang, Y., Xu, S., Hao, F., Lu, Y., Shu, Z., Yan, D., Lu, Y., 2019. Geochemical and petrographic characteristics of Wufeng-Longmaxi shales, Jiaoshiba area, southwest China: Implications for organic matter differential accumulation. *Mar. Petrol. Geol.* 102, 138–154. <https://doi.org/10.1016/j.marpetgeo.2018.12.038>.
- Wu, S., Yang, Z., Zhai, X., Cui, J., Bai, L., Pan, S., Cui, J., 2019. An experimental study of organic matter, minerals and porosity evolution in shales within high-temperature and high-pressure constraints. *Mar. Petrol. Geol.* 102, 377–390. <https://doi.org/10.1016/j.marpetgeo.2018.12.014>.
- Xu, J., Wu, K., Yang, S., Cao, J., Chen, Z., Pan, Y., Yan, B., 2017. Real gas transport in tapered noncircular nanopores of shale rocks. *AIChE J.* 63 (7), 3224–3242. <https://doi.org/10.1002/aic.15678>.
- Xu, J., Wu, K., Li, R., Li, Z., Li, J., Xu, Q., Li, L., Chen, Z., 2019. Nanoscale pore size distribution effects on gas production from fractal shale rocks. *Fractals-Complex Geom. Patterns Scaling Nat. Soc.* 27 (4), 1950142. <https://doi.org/10.1142/S0218348X19501421>.
- Xu, R., Li, H., Guo, C., Hou, Q., 2014. The mechanisms of gas generation during coal deformation: Preliminary observations. *Fuel* 117, 326–330. <https://doi.org/10.1016/j.fuel.2013.09.035>.
- Yan, D.P., Zhou, M.F., Song, H.L., Wang, X.W., Malpas, J., 2003. Origin and tectonic significance of a Mesozoic multi-layer over-thrust system within the Yangtze Block (South China). *Tectonophysics* 361 (3), 239–254. [https://doi.org/10.1016/S0040-1951\(02\)00646-7](https://doi.org/10.1016/S0040-1951(02)00646-7).
- Yang, Y., Aplin, A.C., 1998. Influence of lithology and compaction on the pore size distribution and modelled permeability of some mudstones from the Norwegian margin. *Mar. Petrol. Geol.* 15 (2), 163–175. [https://doi.org/10.1016/S0264-8172\(98\)00008-7](https://doi.org/10.1016/S0264-8172(98)00008-7).
- Zavattieri, P.D., Espinosa, H.D., 2001. Grain level analysis of crack initiation and propagation in brittle materials. *Acta Mater.* 49 (20), 4291–4311. [https://doi.org/10.1016/S1359-6454\(01\)00292-0](https://doi.org/10.1016/S1359-6454(01)00292-0).
- Zeng, L., Zhu, H., Hao, Y., Shi, E., Lu, Y., Qi, Y., 2023. Microstructures and pore structures of naturally deformed shales: Significance for shale gas exploration in the complex tectonic areas of the margin of the Sichuan Basin, South China. *Energy Fuels* 37 (14), 10414–10425. <https://doi.org/10.1021/>

[acs.energyfuels.3c01539](https://doi.org/10.1016/j.fuel.2018.04.137).

Zhang, L., He, C., 2013. Frictional properties of natural gouges from Longmenshan fault zone ruptured during the Wenchuan Mw7.9 earthquake. *Tectonophysics* 594, 149–164. <https://doi.org/10.1016/j.tecto.2013.03.030>.

Zhu, H., Ju, Y., Qi, Y., Huang, C., Zhang, L., 2018. Impact of tectonism on pore type and pore structure evolution in organic-rich shale: Implications for gas storage and

migration pathways in naturally deformed rocks. *Fuel* 228, 272–289. <https://doi.org/10.1016/j.fuel.2018.04.137>.

Zhu, H., Ju, Y., Huang, C., Han, K., Qi, Y., Shi, M., Yu, K., Feng, H., Li, W., Ju, L., Qian, J., 2019. Pore structure variations across structural deformation of Silurian Longmaxi Shale: An example from the Chuandong Thrust-Fold Belt. *Fuel* 241, 914–932. <https://doi.org/10.1016/j.fuel.2018.12.108>.